



日本原子力研究開発機構機関リポジトリ
Japan Atomic Energy Agency Institutional Repository

Title	Ablation plume structure and dynamics in ambient gas observed by laser-induced fluorescence imaging spectroscopy
Author(s)	Miyabe Masabumi, Oba Masaki, Imura Hideki, Akaoka Katsuaki, Khumaeni A., Kato Masaaki, Wakaida Ikuo
Citation	Spectrochimica Acta, Part B, 110, p.101-117
Text Version	Author's Post-print
URL	https://jopss.jaea.go.jp/search/servlet/search?5051841
DOI	https://doi.org/10.1016/j.sab.2015.06.004
Right	© 2015. This manuscript version is made available under the CC-BY-NC-ND 4.0 license http://creativecommons.org/licenses/by-nc-nd/4.0/

Ablation plume structure and dynamics in ambient gas observed by laser-induced fluorescence imaging spectroscopy

M. Miyabe,^{a)} M. Oba, H. Iimura, K. Akaoka, K. Ali, M. Kato, and I. Wakaida

Research Group for Fuel Debris Characterization, Nuclear Science and Engineering Center

Japan Atomic Energy Agency, Tokai-mura, Naka-gun, Ibaraki-ken, 319-1195, Japan

The dynamic behavior of an ablation plume in ambient gas has been investigated by laser-induced fluorescence imaging spectroscopy. The second harmonic beam from an Nd:YAG laser (0.5 - 6 J/cm²) was focused on a sintered oxide pellet or a metal chip of gadolinium. The produced plume was subsequently intersected with a sheet-shaped UV beam from a dye laser so that time-resolved fluorescence images were acquired with an intensified CCD camera at various delay times. The obtained cross-sectional images of the plume indicate that the ablated ground state atoms and ions of gadolinium accumulate in a hemispherical contact layer between the plume and the ambient gas, and a cavity containing a smaller density of ablated species is formed near the center of the plume. At earlier expansion stage, another luminous component also expands in the cavity so that it coalesces into the hemispherical layer. The splitting and coalescence for atomic plume occur later than those for ionic plume. Furthermore, the hemispherical layer of neutral atoms appears later than that of ions; however, the locations of the layers are nearly identical. This coincidence of the appearance locations of the layers strongly suggests that the neutral atoms in the hemispherical layer are produced as a consequence of three-body recombination of ions through collisions with gas atoms. The obtained knowledge regarding plume expansion dynamics and detailed plume structure is useful for optimizing the experimental conditions for ablation-based spectroscopic analysis.

Keywords, Laser ablation, laser-induced fluorescence spectroscopy, plume dynamics, atomic absorption spectroscopy, LIBS

I. INTRODUCTION

In the past few decades, laser ablation has become a key technology having extensive practical and research-oriented applications including pulsed laser deposition (PLD) of thin films [1], ultraviolet (UV) light source for lithography [2], laser-induced breakdown spectroscopy (LIBS) [3], laser-ablation inductively coupled plasma mass spectrometry [4], and fundamental atomic spectroscopy [5], where the ablation plume is produced under various experimental conditions. Accompanying this expansion of the fields of laser ablation application, a significant amount of research on plume characteristics has been conducted mainly by means of laser-induced plasma emission spectroscopy [6]. In emission spectroscopy, a majority of the deduced information pertains to highly excited atoms in a plume. However, for some applications, evaluating the behavior of ground state and metastable atoms (hereafter shortly ground state atoms) in detail is desirable. For instance, many researchers are currently developing LIBS techniques with improved sensitivity utilizing both ground state and highly excited atoms, such as double pulse LIBS [7, 8], combined LIBS and laser-induced fluorescence (LIF) [9, 10], resonant LIBS [11], resonance-enhanced LIBS [12], spark discharge LIBS [13], and microwave-assisted LIBS [14-16]. Additionally, the properties of PLD-produced thin films, such as thickness and stoichiometry, are determined to a great extent by the spatial distribution of ground state atoms because this is a major component of the ablated species in a plume.

Presently, we have investigated various characteristics of ground state atoms in ablation plumes using laser ablation absorption spectroscopy (LAAS) [17-19] to develop remote isotope analysis for highly radioactive nuclear fuels [20-22]. We used a low pressure gas environment because the measurement of highly resolved absorption spectra for ablated species requires a reduction of Stark and pressure broadenings. Because the plume expansion in this case is considerably affected by the ambient gas, it is of great importance to evaluate the spatiotemporal distribution of the ablated species in gas for sensitive analysis. Our previous study revealed

that the absorption spectrum for ablated species splits into two symmetrical peaks under particular experimental conditions, and the splitting interval gradually decreases with time after ablation [20]. From the splitting behavior owing to the Doppler effect, it was inferred that most of the ablated species accumulate in a hemispherical layer at a boundary between the expanding plume and the ambient gas, and that a cavity containing a lower density of ablated species develops in the region surrounded by the layer. Because very few studies have reported such a hollow plume structure, experimental confirmation of the expected distribution and a detailed analysis of the formation of this structure are desirable for applications using the laser ablation technique.

Most previous studies concerning plume structure have utilized emission imaging spectroscopy [23-28]. From the observed emissivity distributions, several researchers have estimated the cross-sectional number density distributions of highly excited atoms using Abel inversion [29-30]. In contrast, for the study of the distribution of ground state atoms in a plume, LIF and absorption imaging techniques have been employed. For example, Gilgenbach *et al.* demonstrated dye-laser resonance absorption photography in the early 1990s [31]. Around the same time, the LIF imaging technique using a sheet-shaped laser beam was introduced to observe the cross-sectional structure of the irradiated portion of a plume [32-35]. Nakata *et al.* compared the expansion characteristics of ground state and highly excited atoms using fluorescence and emission imaging spectroscopy [36].

As described above, resonant fluorescence imaging spectroscopy is considered to be a powerful and established technique for the characterization of plume internal structure. Nevertheless, to our best knowledge, no applications of this technique to the detailed study of plume structure evolution have been published, with the exception of some partial observation reports [29, 36, 37].

Therefore, in the present study we employ LIF imaging spectroscopy to investigate ablation plume characteristics in low pressure gas ambient, with particular attention to the formation of the previously expected hemispherical thin layer and internal cavity containing a reduced density of ablated species [20]. Gadolinium was chosen as a target sample since it can be handled easier than nuclear fuel materials and also is a lanthanide having similar electronic structure to actinide. From the present study, we will verify that this

structure is actually formed in the plume, and propose a mechanism for the formation of this structure. Furthermore, we will discuss how the sensitivities of LAAS and LIBS analyses are influenced by the plume structure.

II. EXPERIMENTAL

Figure 1 shows an experimental setup for LIF imaging spectroscopy. The second harmonic radiation from an Nd:YAG laser (Spectra Physics, INDI-10, 532 nm, 8 ns) was delivered to a vacuum chamber, and then focused normally on a target sample with a lens of 200 mm focal length. Typically a sintered oxide pellet (Rare Metallic, 10 mm ϕ , 10 mm thickness, 99.9%) was used as a sample, whereas in the measurement of chemical state dependence a metal chip of gadolinium (High Purity Chemicals, 10 mm \times 10 mm, 1 mm thickness, 99.9%) was also utilized. The lens-sample distance was adjusted to place the focal point at a position approximately 1 mm behind the surface of the irradiated sample. The sample stage was rotated at a rate of about 2 rpm to avoid the crater effect. The pulse energy was normally set to 0.5 mJ (fluence: 1.5 J/cm²); in the measurement of ablation energy dependence the energy of 0.15 mJ was also examined. The pulse energy was monitored during measurements using a pyroelectric detector (Ophir PE-30), and was adjusted by rotating the linear polarization angle of the beam with respect to a polarizing beam splitter cube using a half-wave plate.

Helium (purity 99.99%) was typically employed for the ambient gas, but two other gases (argon and xenon: purity 99.99% each) were also employed individually for the ambient gas. After evacuating the chamber with a vacuum pump and flushing several times with the gas, the chamber was filled with the gas, and the pressure was maintained constant owing to continuous pumping and gas flow. The LIF images were acquired in helium ambient at a pressure of 800 Pa unless described otherwise. The pressure was monitored with a capacitance manometer (MKS, Baratron) for lower pressure and a convection-enhanced Pirani gauge (Granville-Phillips, 475series) for higher pressure, and the flow rate was controlled with a flow regulating valve.

The produced ablation plume was subsequently intersected with a probe beam from a tunable dye laser (Sirah, Cobra-Stretch, DCM dye) that was equipped with a harmonic generator (BBO) and was pumped by

another Nd:YAG laser (Spectra Physics, INDI-10). The UV probe beam was first expanded with a quartz concave lens (focal length: -250 mm) and then converted into a thin sheet-shaped beam by passing through a slit (gap width: 0.5 mm) located in front of the sample to avoid generating interference fringes. The fluence at the sample stage was set at approximately 2 mJ/cm². The wavelength of the dye laser was monitored with a wavemeter (Coherent, WaveMaster). When the dye laser was tuned to the resonance wavelengths of the gadolinium atoms and ions, fluorescence was emitted from the portion of the plume irradiated by the probe beam. In the present study, we chose two intense excitation transitions both originating from the ground states of Gd atoms and ions, as shown in fig. 2. Many relaxation transitions arise from these excited states, as listed in Table 1. The fluorescence transitions used to measure the images for atoms and ions shown in fig. 2 were chosen considering the magnitude of the branching ratio and the wavelength difference from the excitation transition.

LIF images were obtained using an intensified CCD (ICCD) camera (Andor, DH334T-18F-03) from a direction orthogonal to the probe beam. The spatial resolution of the image is estimated to be around 100 μ m considering pixel size of the camera and an error in focus adjustment. Placing an interference filter (passband: 10 nm, transmission: 16.5 % at 346.899 nm for the 350 nm-band filter, 30.0 % at 476.383 nm for the 480 nm-band filter) in front of the camera, LIF images with higher contrast were obtained by blocking the plasma emission from the plume and stray light from the YAG lasers. For measurement of the UV fluorescence image, UV grade optics (lens, windows, and mirrors) were used between the camera and the plume. According to the camera specification sheet, the sensitivity of the ICCD camera at 480 nm is higher than that at 350 nm by factor 1.7 .

Figure 2 also shows a schematic of the firing timing of the ablation and probe lasers along with the gate timing of the camera. These timings were controlled using a multichannel delayed pulse generator (SRS, DG645). The plume observation timing was adjusted by varying the delay time between the 8 ns probe pulse and the 8 ns ablation pulse generally in the range 0.1 – 5.0 μ s. Additionally, from a preliminary experiment, the delay of the camera gate from the onset of the probe laser irradiation and the gate width were optimized to be 10 ns and 100 ns, respectively.

We used the image processing software package (Andor, SOLIS) for analysis of the acquired images. Despite the use of interference filters with 10 nm passbands, several plasma emission lines lie in the narrow transmission band. For examples, table 2 summarizes ten of the most intense emission lines transmitted through the filters utilized. Hence, we imaged the plasma emission alone by blocking the probe laser beam after obtaining LIF images; by subtracting the emission image from the corresponding LIF image using the image processing software, higher contrast LIF images were obtained. The typical emission intensity was an order of magnitude lower than the fluorescence intensity.

Figure 3 shows the calculated absorption spectra for the Gd I 313.692-nm line together with the measured spectral profile of the dye laser. These absorption spectra were calculated from the natural isotope abundance and the reported isotope-shift data [38] considering the relative isotope shift factors [39, 40]. Generally the absorption spectrum for ablated species becomes narrower at larger delay time from ablation owing to the reduction of Stark and Doppler broadenings. In this figure, absorption spectra with Gaussian linewidths of 5 GHz (b) and 1 GHz (c) are shown as examples at smaller and larger delay time from ablation. At smaller delay time, the resonances for all isotopes overlap to form a single broad peak. On the other hand the dye laser bandwidth was measured to be about 3 GHz using a solid etalon (Free Spectral Range: 12 GHz, Finesse: 20). From the cavity length of about 40 cm, the longitudinal mode spacing of the dye laser is estimated to be 0.37 GHz. Since the absorption profile contains more than 8 longitudinal modes, the dye laser can be treated as a quasi-continuum light source [41].

III. RESULTS AND DISCUSSION

3.1. Wavelength dependence on LIF images

To confirm that the observed LIF image arises from the expected transition, we first acquired images by scanning the probe laser wavelength near the atomic transitions shown in fig. 2 in increments of 0.002 nm. Figure 4 shows the LIF images for Gd atoms and ions obtained at four different delay times, where the images labeled with “0 nm” were acquired with a probe laser beam tuned to the resonant wavelength. In these figures,

the rightmost images were acquired with the longest wavelength of the probe laser and vice versa. Figures 4(a) and (c) show the plume at early stages of evolution for delay times of 0.3 and 0.5 μs , respectively, whereas (b) and (d) show the later stages for delay times of 0.7 and 1.5 μs , respectively. The actual physical size of each image is approximately 9 mm \times 9 mm. From these figures it is found that the images have higher contrast in comparison with the plasma emission. Also, in these figures, the bright portion of the image and the brightness of the plume vary with varying probe laser wavelength, indicating that the observed LIF images must arise from the transitions of interest.

As expected from our previous study, the ablated ground state atoms and ions accumulate in a hemispherical boundary layer between the plume and the ambient gas, and a cavity containing a lower density of ablated species is formed in the region surrounded by the layer, particularly at later stages. When the laser detunes to a shorter wavelength, the left side (the downstream side) of the plume becomes brighter. In contrast, when detuning to a longer wavelength, the right side (the upstream side) of the plume becomes brighter. Thus, this variation in the luminous portion is attributed to the Doppler effect. It should be noted that this variation is more remarkable for early images of the plume ((a) and (c)). This indicates that plume expansion is only slightly decelerated by the ambient gas at early stages, whereas expansion nearly stops at a delay time of 1.5 μs .

From the images acquired with the resonance light (0 nm), it is clear that the rightmost and leftmost parts of the plume, having large opposite horizontal velocities can be simultaneously excited by the probe laser beam tuned to the center wavelength of the resonance even at an earlier stage. This indicates that the bandwidth of the dye laser utilized and the absorption linewidth of the Gd transitions are sufficiently large in comparison with the Doppler effect arising from the expansion velocity of the plume under the present conditions.

3.2. Temporal evolution of plume structure for the Gd oxide sample

Figure 5 shows the temporal evolution of the plume structure in the delay time range of 0.2–5.0 μs obtained under equivalent experimental conditions of those for fig. 4. For comparison, each LIF image is normalized by its own maximum intensity, whereas, in actuality, the intensity rapidly decreases with time.

These figures indicate that the plume structure of atoms is more complicated than that of ions. For the atomic plume shown in fig. 5(b), the presence of an outer layer having a characteristic hemispherical shape becomes visible from 0.3 μs and pronounced around 0.6 μs , whereas a more luminous and isotropically expanding component appears close to the surface even at 0.2 μs . This inner component expands more rapidly in the cavity than does the outer layer so that the two begin to coalesce at around 1.5 μs . In the case of the ionic plume shown in fig. 5(a), both the hemispherical layer and the inner luminous component are observed at 0.2 μs . Furthermore, the inner component propagates more rapidly in the surface normal direction than does the inner component of the atomic plume so that it coalesces into the hemispherical layer earlier, at around 0.5 μs . To the best of our knowledge, this hemispherical layer formation and the different behaviors for ionic and atomic plumes are shown here for the first time, whereas the plume splitting and coalescence have been reported by several researchers [1, 23, 26]. The formation of a hemispherical layer for ionic and atomic plumes is considered to arise from the ion–electron recombination process for doubly and singly charged ions, respectively, which will be discussed later.

At a later expansion stage shown in this figure, the plume boundary becomes unclear and shrinks slightly prior to its disappearance. According to Monte Carlo simulations of plume dynamics [42], it has been shown that, after plume expansion ceases, the plume boundary shrinks slightly owing to the overexpansion effect and again starts to expand (plume oscillation) [43, 44]. Thus, the observed shrinkage can be interpreted as this behavior. However, this figure also shows that the atomic plume begins to shrink at a later time than the ionic plume. This temporal difference is difficult to explain using a simple hydrodynamic mechanism. The difference may be caused by the escape of charged species from the plume through Coulombic repulsion.

Figures 6 and 7, respectively, show the fluorescence intensity distributions along the surface normal (longitudinal) and the horizontal (lateral) axis at a 0.5 mm height relative to the sample surface. These profiles

were obtained from fig. 5 by averaging the data over a 150 μm width along each axis to improve the signal-to-noise ratio. In fig. 6, all plots were drawn according to a common intensity scale; thus, the intensity variations can be compared throughout the progression of plume evolution. However, in fig. 7, the intensity was normalized by its maximum value for each plot to readily identify the peaks.

As shown in fig. 6, the fluorescence signal derived from the hemispherical layer for ions is slightly more intense than that for atoms. Considering the branching ratios, the detection sensitivities of the camera and the transmissions of the filters for the atomic and ionic fluorescence transitions, the maximum population of ions in the ground state at 4 mm and 1 μs is estimated to be approximately 2.3 times larger than that of atoms at 4.5 mm and 3 μs . This larger population of ions is consistent with the interpretation that the recombination is a dominant process for forming a hemispherical layer.

In this estimation, the difference in the oscillator strengths for the excitation transitions was neglected because the excitation transitions were almost saturated under the present conditions. Figure 8 shows a typical saturation characteristic for the Gd II 309.865-nm line. The similar curve was also measured for the Gd I 313.692-nm line. This curve was obtained by averaging the LIF intensity in the area of $300 \times 300 \mu\text{m}^2$ around the center of the plume from the images measured with various fluences of the probe laser at a delay of 1 μs . From this figure, it is found that the fluence of 2 mJ/cm^2 , at which the LIF images were acquired, is enough to saturate this transition. The slight signal variation at this fluence most likely occurs because the absorption spectrum is broader than the laser bandwidth as shown in fig. 3.

In this figure, the intensity of the inner component of atoms decreases rapidly in the delay time range of 0.2–0.8 μs . However, considering the increase in the volume of this component during this period, it is evaluated that the spatially integrated fluorescence intensity is increasing rather than decreasing. The most probable mechanism for producing atoms in the inner component is the dissociation of gadolinium oxide molecules directly released from the sample surface. This speculation is supported by the different behaviors of the inner components observed for the metal samples, which will be described later.

Figure 7 is noteworthy in that the intensity distribution of atoms exhibits a sharp outward edge, whereas that of ions exhibits a long tail having a gentle slope beyond the intensity peak at the hemispherical layer. This

difference can be explained if we assume that the principal neutralization process of ions is the three-body recombination, requiring simultaneous collisions with ions, electrons and gas atoms, as discussed later. Generally a majority of the species directly ablated from sample surface are ions and the ions expand faster than neutral atoms. Thus we consider the collisions of ions with gas atoms in the contact layer, having higher density of the species.

The ions escaping heavy collisions with gas atoms are not significantly decelerated and not neutralized. Thus they are distributed over extensive distance from the layer, leading to the intensity distribution having a long and gentle slope as shown in fig. 7(a). On the other hand, the ions once heavily collided with gas atoms are further decelerated owing to the subsequent multiple scattering, because they are unable to escape from the contact layer and the scattering cross section increases with decreasing particle velocity. Since the recombination rate also increases with decreasing the velocity, slower ions tend to be neutralized with higher rate. Thus many of the slow atoms are produced in the hemispherical layer whereas few atoms appear outside of the layer, which makes the slope outside of the layer steeper than inside as shown in fig. 7(b).

Features similar to the intensity distributions observed for atoms and ions are also observed in the emission images arising from highly excited species. Figure 9 shows four emission images obtained in the absence of the sheeted probe beam with a camera exposure time of 100 ns. Each image is normalized by its own maximum intensity to facilitate comparison with the images given in fig. 5. As listed in Table 2, some of the emission lines of highly excited ions and atoms are transmitted through the 350 nm and 480 nm filters, respectively. Thus, the emission images can be used to distinguish the spatial distributions of these species. The excited ions shown in fig. 9(b) are loosely distributed around the plume periphery, whereas the distribution of the excited atoms in fig. 9(a) is limited to the region surrounded by the hemispherical layer. Because this emission image is not a cross-sectional view of the plume, unlike the LIF images, it is unclear whether the excited atoms exist only within the layer or also within the cavity. However, the differences in these emission images further supports our speculation because recombination produces many highly excited atoms (most probably Rydberg atoms), which subsequently decay to the ground state through cascade relaxation, and there are few excited atoms outside the layer.

3.3. Ablation pulse energy dependence

The plume structure varies with the pulse energy of the ablation laser. For ablation-based spectroscopic analysis, a pulse energy range of 0.1–10 mJ is considered to be most appropriate. Thus, we further acquired LIF images for pulse energies of 0.15 mJ (0.5 J/cm^2) and 2 mJ (6.7 J/cm^2) with all other experimental conditions being equivalent to those for fig. 5. The obtained results are shown in fig. 10, and the longitudinal and lateral intensity profiles for the condition of 0.15 mJ irradiation are shown in figs. 11 and 12, respectively. For comparison, the intensity scale of fig. 11 is matched with that of fig. 6.

From fig. 11(a), it is clear that the plume size is smaller, and the intensity decreases more rapidly, particularly for ions, relative to the data presented in fig. 6(a). In the case of fig. 6(a), the intensity around the hemispherical layer is nearly constant in the delay time range 0.3–1.0 μs , suggesting that the production of ground state ions through recombination and subsequent relaxation from doubly charged ions is predominant. In contrast, the intensity in fig. 11(a) decreases monotonically. Thus, this difference suggests that fewer doubly charged ions are produced in the plume for 0.15 mJ irradiation.

It is noteworthy that the intensity around the hemispherical layer for atoms ablated with lower pulse energy (fig. 11(b)) is slightly higher than that with higher energy (fig. 6(b)). This can be interpreted as follows. If the ablation energy increases, a larger number of higher excited and higher charged species are produced in comparison to the ground state atoms. Some of these can decay back to the atomic ground state through recombination and/or cascade relaxation processes, whereas the remaining component is lost during these processes through clustering or oxidization. Because a cascade relaxation rate is generally low, this lengthens plume persistence time but reduces fluorescence intensity. Moreover, as shown in figs. 5 and 10, the plume size increases considerably with increasing ablation energy. Thus, while the total amount of ablated species increases with increasing ablation energy, the number density of ground state atoms in the hemispherical layer increases to a lesser extent.

This fact influences the optimum choice of ablation energy for LAAS and LIBS analyses as well, but does so differently for the two methods. LAAS analysis measures the line-of-sight absorption over a limited portion of the plume. Because the measured quantity is proportional to the number density of ground state atoms, the absorption signal increases to a lesser extent than does the total amount of ablated species with increasing ablation energy. In contrast, for LIBS in which the emission can be integrated over the entire plume for the entire duration, higher analytical sensitivity can be achieved for higher ablation energy. This finding is of practical importance for LAAS because minimum necessary ablation energy (~ 0.15 mJ) can avoid releasing large fragments from the sample, enabling more precise analysis with lower sample consumption.

From figs. 10(c) and (d), it is apparent that the plume size is larger and that an observable LIF intensity is retained for a longer duration (up to $30 \mu\text{s}$) for the 2.0 mJ irradiation case. Additionally, the plume structure at an earlier stage is still similar to that shown in fig. 5, whereas the inner structure becomes unclear at a later stage. With increasing ablation energy, larger fragments tend to be released from the surface, which increases the shot-to-shot fluctuation of the plume structure. The obscuration of the plume structure observed for 2 mJ irradiation is, therefore, partly due to the averaging of the highly fluctuating plume images obtained over 60 laser shots. From this result, it is suggested that the plume structure given in figs. 5 and 10 should be considered for the development of sensitive LIBS as well as LAAS.

3.4. Fluorescence intensity peak analysis using theoretical models

Sensitive analysis using ablated ground state atoms requires knowledge of the peak position of the density distribution. Figure 13 shows the temporal variations in the distance of the fluorescence peak from the ablation spot evaluated from figs. 6 and 7. Figures 13(a) and (b) show these temporal variations for the longitudinal direction, whereas fig. 13(c) shows those for the lateral direction at a 0.5 mm height from the sample surface. In figs. 13(a) and (c), open and filled symbols represent the hemispherical layers for atomic and ionic plumes, respectively, whereas fig. 13(b) shows the inner component for atomic plume. In these figures, the data for various pressures other than 800 Pa are also included to examine the pressure dependence. These figures

indicate that the outer hemispherical layer of atoms appears at nearly the same location as that of ions for various pressures in both directions, except that the lateral size of the ionic layer is slightly larger than that of the atomic layer under lower pressure conditions (fig. 13(c)). The reasonable agreement between the ionic and atomic layer locations indicates that neutral atoms in the layer are produced from singly charged ions through an ion–electron recombination process.

For analysis of these distance–time plots, the drag force model and the blast wave model are frequently employed. Because the validity of the drag model has been verified for ablated species heavier than gas atoms [23, 45], the measured distance from the ablation spot was fit to the following equation:

$$d = d_f (1 - e^{-\beta t}), \quad (1)$$

where d_f and β denote the stopping distance and the slowing coefficient, respectively. Because of the general agreement of the outer layer locations for atomic and ionic plumes, we considered their averaged locations in this analysis. Table 3 summarizes the parameters determined by fitting the data in fig. 13 to the drag model given by equation (1). The estimated error for most of the parameters is around 10%, whereas that for the inner component is larger. The smaller slowing coefficients for the inner component indicate that the component can propagate more smoothly in the cavity; similar behavior has also been reported in literature [26]. When the shockwave is generated during plume expansion, the ablated material pushes the ambient gas away from the sample as a piston so that the gas in the plume becomes rarefied (i.e., the snowplow effect) [46-48]. The smooth propagation of the inner component suggests that the developed cavity is filled with not only few gas atoms, but also few species which cannot be detected with the LIF imaging spectroscopy, i.e. molecules, clusters, etc. at least during an expansion stage of the inner component. This interpretation is also supported by the study of Yamagata *et al*, which revealed that the pressure inside the plume is lower than that of the surrounding gas especially close to the target surface [49].

As is often pointed out, the estimated d_f value is roughly an order of magnitude larger than the elastic mean free path [50-52]. Thus, to check the validity of the obtained d_f values, a scattering cross-section (σ) was estimated using the following relation, by assuming that the stopping distance is five-fold of the mean free

path of ablated species in an He ambient:

$$\sigma = \frac{5}{d_f n_g}, \quad (2)$$

where n_g denotes the number density of gas atoms. From the longitudinal and lateral expansion parameters of the outer layer, the cross-sections were determined to be 0.8×10^{-16} and 1.0×10^{-16} cm² for Gd ions with kinetic energies of 75 and 33 eV, respectively. These values are consistent with the order of magnitude of the reported cross-section for the collision of Ag ion with He atom [52] as well as the geometric cross-section of atoms given as πa_0^2 ($= 0.88 \times 10^{-16}$ cm²), where a_0 is the Bohr radius.

The parameters for lateral expansion under 0.15 mJ irradiation are also listed in Table 3. These values are in plausible agreement with those determined from the Doppler splitting effect on the absorption spectra for cerium ions ($d_f = 1.8$, $\beta = 2.0$) in our previous study [20]. This agreement suggests that the Doppler splitting of absorption spectra for ablated ionic species was originated from the expanding motion of the hemispherical layer which is similar to that shown in fig. 10(a). On the contrary, the Doppler splitting for neutral species reported in our previous study was most probably originated from the expanding motion of the inner component of the atomic plume.

As described above, the drag model is suited for the analysis of our present data; however, it is difficult from the analysis based on this phenomenological model to obtain a more detailed understanding of the underlying physical mechanisms that govern the plume expansion dynamics and the properties of the plume. In the last few decades, numerous efforts have been made to construct more general physical models for plume expansion into ambient gas under various pressures [53-55]. In the model proposed by Predtechensky and Mayorov (PM), an infinitely thin hemispherical layer (of radius d) that expands into ambient gas while experiencing a force due to the ambient gas pressure (P_g) is considered. It is assumed that the layer contains both masses of confined plume species (M_p) and displaced gas species ($(2/3)\pi\rho_g d^3$, where ρ_g is the gas density given as 0.17 kg/m³ for He). The expanding velocity at a radius d ($u(d)$) derived from the equation of motion considering the balance between the momentum variation in the outer layer and the external pressure force is given as follows:

$$u(d) = c_0 \sqrt{\frac{b^2}{(a^3 + d^3)^2} - 1}, \quad (3)$$

for

$$a = \left(\frac{3M_p}{2\pi\rho_g} \right)^{\frac{1}{3}}, \quad b \approx a^3 \left(\frac{u_0}{c_0} \right), \quad c_0 = \sqrt{\frac{P_g}{\rho_g}},$$

where u_0 and c_0 denote the initial expansion velocity and the sound velocity in the ambient gas, respectively.

To determine the parameters a and b for each pressure for the longitudinal expansion of the layer, we first calculated, from fig. 13(a), the expansion velocity as a function of the distance, and then the plots of the velocity and the distance were fit to equation (3). Furthermore, using the determined parameters, the differential equation (3) was numerically integrated under the initial condition $d(t = 0) = 0$ so as to obtain the distance–time profile. Figure 14 shows a typical resultant profile in accordance with the measured data. In this figure, all data were expressed using the following dimensionless coordinates:

$$\text{dimensionless distance: } \zeta = d / a,$$

$$\text{dimensionless time: } \tau = tc_0 / a.$$

The solid curve in fig. 14 represents the profile calculated using the PM model for the case of 500 Pa ($M_p = 5.4 \mu\text{g}$, $u_0 = 9.9 \text{ km/s}$). As shown in this figure, all the measured points fall along a single curve, although there are some deviations. In the dimensionless coordinates used, the point at $\zeta = 1$ corresponds to the condition where the mass of the displaced gas is equal to the plume mass and the expansion exhibits point blast dependence. It should be noted that this PM model is constructed by assuming that (i) the secondary shockwave is formed as a result of deceleration of the primary outward shockwave in ambient gas, and (ii) the plume species and the displaced gas species are separately concentrated in two thin layers sandwiched between these shockwaves wherein the layers are in direct contact through a common interface. The good agreement between the measurements and the model suggests that these assumptions are well satisfied for the observed plume. In the present case, the atomic weight of the plume species is considerably greater than that of the gas species (i.e., $M_{\text{Gd}}/M_{\text{He}}$ is ~ 40). Thus, the ablated species propagates closely with the contact surface until the later stages of evolution, which probably makes the assumption of an infinitely thin layer valid for a longer duration than

under conditions where the mass of the ablated species more closely matches that of the gas species.

3.5. Temporal evolution of the plume structure for the Gd metal sample

LIF images were also acquired using a Gd metal sample under equivalent experimental conditions as were employed for the oxide sample to evaluate how the plume structure depends on the chemical properties of the sample. The obtained images are shown in fig. 15, and the fluorescence intensity distributions along the surface normal direction are given in fig. 16. Slightly larger, yet similar hemispherical layers were also observed for the metal sample. In comparison with the oxide sample, the most notable difference is the behavior of the inner component of the plume. The inner components of both atoms and ions are in contact with the metal surface during the early stages. This is presumably because the metal surface is still hot, and the ground state atoms and ions of Gd are continuously released even at around 0.5 μs after ablation. The inner component gradually diffuses in the cavity and vanishes, forming a simple plume structure. The observed monotonic decrease in the density of the inner component suggests that there is no additional production of atoms through dissociation of oxide molecules for the ablation of metal samples. The fact that the plume for the metal sample is slightly larger than that for the oxide sample can be also explained by the absence of the additional energy consumption required to dissociate oxide molecules.

It is worth noting that the hemispherical layer of atoms for the metal sample is considerably thinner; for example, the thickness at a delay time of 1 μs is estimated to be 500 μm (full width at half maximum) from fig. 16(b). Additionally, careful attention to the plume evolution shown in fig. 5(b) indicates that the thicker outer layer for the oxide sample arises from the coalescence of the inner component with the outer layer; thus, the outer layer of atoms is probably thin regardless of the chemical state of the sample. This small thickness indicates that recombination occurs in a very narrow region wherein the density of ablated species attains a value higher than 5×10^{17} atoms/cm³ considering the mass of the plume species (M_p) determined in Section 3.4. In the following section, we will discuss how the thin layer and the cavity form, with particular attention to the interaction between the ablated and gas species.

3.6. Dependence of the plume structure on gas conditions

To investigate the role of the ambient gas on the formation of the plume structure, we obtained LIF images under conditions of varying helium gas pressure. Figure 17 shows the plume images obtained at a delay time of 0.5 μs for various pressures in the range 10 Pa to 13.2 kPa. In the case of ablation in a vacuum, approximately two components having different velocities appear [22]. One of these is a faster component arising from ionic species accelerated with the potential double layer [56], which is built up by electrons escaping from the initially generated plume and in which there is an electric field outwardly attracting positive ions. The other is a slower component arising from the atoms and ions both which are accelerated solely by the Knudsen layer effect [57]. The pressure dependence shown in fig. 17 indicates that the slower atomic component and the faster ionic component in vacuum turn into the inner components of atoms and ions in the gas, respectively, and the outer layers in the gas are missing in the plumes in vacuum for both the species. This suggests that a charge decrease process such as the neutralization of ions is prompted by a collisional interaction with ambient gas.

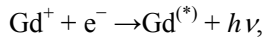
Furthermore, fig. 17 shows that the fluorescence intensity distribution varies from unidirectional to isotropic with increasing gas pressure, whereas a majority of ablated species move in a direction normal to the surface in a vacuum. This suggests that the initial unidirectional kinetic energy of the plume is converted to an isotropic distribution as a result of multiple scattering between the ablated and gas species, resulting in the formation of the hemispherical plume boundary. Because the plume size approaches the spatial resolution of the image, the hemispherical layer becomes unclear at a pressure higher than 5 kPa. Moreover, for a higher pressure region, owing to the intense plume confinement, the number density of the ablated species and their collision frequency increase; thus, the plume is probably homogenized more rapidly. According to the latest emission imaging studies, however, the internal structure is still observed even for a plume under atmospheric pressure [58]. The mechanism by which the structure forms is reported to be mainly due to the plasma shielding effect, which is different from the lower pressure ambient case. Because the knowledge of the plume structure under

atmospheric pressure is of practical importance for LIBS and LAAS [59], it is desirable to examine more detailed structure variation between vacuum and atmospheric pressure.

Finally, to study the influence of the atomic weight of the gas on the plume structure formation, LIF images were acquired at a delay time of 1 μs using three gases (He, Ar, and Xe), as shown in fig. 18. The pressure of each gas was chosen to produce nearly equivalent final plume sizes. From fig. 18, it is clear that the cavity size is larger for lighter gases. This structure variation relative to the mass of the ambient gas can be interpreted as follows. In the case of Xe, because of the small difference in the atomic weights between Gd and Xe, the Gd atoms and ions lose a majority of their initial kinetic energy although they engage in only a few elastic collisions with Xe atoms and some of them are backscattered as well. The Gd species that lose their kinetic energy during plume expansion come to rest near the locations where collisions occurred, producing a thicker hemispherical layer for both atoms and ions, as shown in the right-most column of fig. 18. In contrast, in the case of He, owing to its considerably smaller atomic weight, the Gd species lose less kinetic energy through an elastic collision with He atom. In this case, until the plume loses its expansion energy, most of the ablated species continue to displace the surrounding gas, which produce a thinner hemispherical layer and a larger cavity, as indicated by the left-most column of fig. 18.

In general, neutralization of ions in plasma occurs through four types of ion–electron recombination processes as follows [60].

(1) Radiative recombination [inverse process of ionization to a continuum]:



(2) dielectronic recombination [inverse process of autoionization]:



(3) three-body collisional recombination:



(4) dissociative recombination:



where Gd^* and Gd^{**} denote the excited state and the doubly excited autoionizing state, respectively.

As discussed above, many of the results obtained in the present study (i.e., the sharp outward edge of the intensity distribution of atoms, the cavity size variation with respect to the mass of the gas, etc.) suggest that the recombination occurring around the hemispherical layer is affected by a collisional interaction of ablated species with gas atoms. Of the four reactions listed above, the three-body recombination (TBR) reaction is accelerated most by the existence of gas atoms [26, 61, 62]. In this recombination, gas atoms as well as free electrons can act as a third body, carrying away the excess energy of this reaction.

The reaction rate of TBR is roughly proportional to the particle densities and is inversely proportional to the electron temperature [60]. For ablation in ambient gas, a large number of energetic electrons are generated through gas breakdown as well as ionization of the ablated species. Its kinetic energy is thermalized through multiple collisions with gas atoms, resulting in a formation of an electron distribution confined around the plume [63, 64]. Thus dense and low-energy electrons are expected to exist at the contact layer between the plume and the gas.

On the other hands, around the hemispherical layer, as discussed in Section 3.4, ablated species propagating with a shockwave and the gas atoms displaced by the plume are separately concentrated in two thin layers separated by the contact surface. Nevertheless, according to the hydrodynamic model, which considers the diffusion across the contact surface, it is expected that these species can be mixed in the region of which thickness is several hundred micrometers [24, 42, 46- 48]. In the mixing region these species are expected to be significantly compressed by the expanding pressure of the shockwave and the resistance of the surrounding gas. As a consequence of this compression in the mixing region, the reaction rate of TBR is most probably enhanced around the contact surface of the expanding plume in ambient gas.

The present study clearly indicates that the distribution of ablated ground state atoms in ambient gas has the characteristic internal structure. Several plume dynamics models assuming a hemispherical thin layer containing mass of all ablated species have demonstrated good agreement with measurements. However, the distribution of the ablated species assumed in the models was not necessarily confirmed experimentally. Thus, the information obtained from the present LIF images will be useful also for further improving theoretical models of plume dynamics in ambient atmosphere.

IV. CONCLUSION

To obtain higher detection sensitivity and analytical precision for LAAS and LIBS analyses, we evaluated the LIF images of ablation plumes. From temporal variations and the gas dependences of the plume, the following characteristics were revealed.

- i) As expected from a previous study on the Doppler splitting of absorption spectra, ablated ground state species tends to accumulate in a hemispherical layer between the plume and the ambient gas, and near the center of the plume, a cavity containing a reduced density of ablated species is formed.
- ii) At an earlier stage of plume evolution, another expanding component appears in the cavity that later coalesces into the hemispherical layer at a delay time of around 0.5 μs for ions and 1.5 μs for atoms.
- iii) The thickness of the hemispherical layer is around 500 μm at a delay time of 1 μs and the number density of ablated species in the layer is estimated to be higher than 5×10^{17} atoms/cm³.
- iv) The hemispherical layer of atoms appears at a nearly identical location as that of ions. This agreement indicates that the ground state atoms in the layer are produced through ion–electron recombination and subsequent relaxation.
- v) The cavity size increases with a decreasing atomic weight of the ambient gas.
- vi) The measured temporal variation in the intensity peak position was satisfactorily fitted with the plume expansion model proposed by Predtechensky and Mayorov.
- vii) From these results, it was inferred that three-body recombination in a significantly compressed mixing region around the contact layer is the dominant mechanism for forming a thin hemispherical layer and an internal cavity.

The knowledge obtained in this study is considered to be of importance for various applications using laser ablation as well as for optimizing experimental conditions for LAAS and LIBS analyses.

Figure caption

Figure 1 Experimental setup for LIF imaging spectroscopy. VP, PG, CM and AT mean vacuum pump, convection-enhanced Pirani gauge, capacitance manometer and attenuator consisting of polarizing beam-splitter cube and half-wave plate. LIF images of ablation plume were acquired with an ICCD camera from an orthogonal direction to the planar probe beam.

Figure 2 Excitation and fluorescence transition schemes of Gd (upper), and laser firing and camera gate timings (lower).

Figure 3 Measured dye laser spectral profile (a) and absorption spectra calculated for the Gd I 313.692-nm transition with Gaussian linewidths of 5 GHz (b) and 1 GHz (c). Each isotope resonance was calculated based on its natural isotope abundance and the reported isotope-shift data considering the relative isotope shift factors. The measured dye laser bandwidth is about 3 GHz.

Figure 4 LIF images acquired with various wavelength near resonances shown in fig. 2 for Gd ions at delay times of 0.3 μs (a) and 0.7 μs (b), and Gd atoms at delay times of 0.5 μs (c) and 1.5 μs (d). Ablation was accomplished under an 800 Pa He ambient and ablation energy of 0.5 mJ using Gd oxide sample. Here “0 nm” indicates that the plume was observed with resonance wavelength of each species.

Figure 5 Temporal evolution of the ablation plume for ions (a) and atoms (b) in the ground states using a Gd oxide sample under an 800 Pa He ambient and ablation energy of 0.5 mJ.

Figure 6 Longitudinal fluorescence intensity distributions for ions (a) and atoms (b) obtained from fig. 5. All plots were drawn using a common intensity scale, and the intensity variation can therefore be compared throughout the plume evolution.

Figure 7 Lateral fluorescence intensity distributions at a 0.5 mm height from the sample surface for ions (a) and atoms (b) obtained from fig. 5. The intensity scale of each plot was normalized by its own maximum value to readily identify the peaks.

Figure 8 Typical saturation characteristic for the Gd II 309.865-nm transition. This curve was obtained by averaging LIF intensity in the area of $300 \times 300 \mu\text{m}^2$ around the center of the plume from the images measured with various fluences of the probe laser at a delay of 1 μs . Other experimental conditions are the same as those for fig. 5. At the fluence of 2 mJ/cm^2 this transition is almost saturated. The slight signal variation at this fluence most likely occurs because the absorption

linewidth is broader than the laser bandwidth.

Figure 9 Typical plasma emission images measured under conditions equivalent to those for fig. 5 in the absence of a sheeted probe beam. In each image, the intensity is normalized by its maximum intensity to facilitate comparison with the images given in fig. 5, whereas the actual emission intensity is typically an order of magnitude lower than the fluorescence intensity. This image is not a cross-sectional view of the plume, unlike the LIF images.

Figure 10 Temporal evolution of the ablation plume for ions and atoms for 0.15 mJ and 2.0 mJ irradiation using a Gd oxide sample under an 800 Pa He ambient. Plume structures similar to those shown in fig. 5 are observed in the pulse energy range of 0.15–2.0 mJ at earlier stages of the evolution. In contrast to the larger differences in plume size and duration for various ablation pulse energies, the difference in fluorescence intensity is not particularly large.

Figure 11 Longitudinal fluorescence intensity distributions for ions (a) and atoms (b) using a Gd oxide sample under an 800 Pa He ambient and ablation energy of 0.15 mJ. The intensity scale is equivalent to that shown in fig. 6 for comparison. The intensity around the hemispherical layer for ions decreases monotonically, whereas it is nearly constant in the delay time range 0.3–1.0 μs shown in fig. 6(a). Furthermore, the intensity around the hemispherical layer for atoms shown in fig. 11(b) is slightly larger than that shown in fig. 6(b).

Figure 12 Lateral fluorescence intensity distributions at a 0.5 mm height from the sample surface for ions (a) and atoms (b) using a Gd oxide sample under an 800 Pa He ambient and ablation energy of 0.15 mJ.

Figure 13 Temporal variation in the intensity peak location for 0.5 mJ irradiation for Gd oxide sample. (a) outer layer along the surface normal, (b) inner component along the surface normal (c) outer layer at a height $d = 0.5$ mm. Open and filled symbols represent peak locations for atomic and ionic plumes. Solid curves represent the best fit of the measured data with the drag model.

Figure 14 Temporal variation in the intensity peak location for various pressures of He ambient using dimensionless coordinates calculated from fig. 13(a). The solid curve represents the profile calculated using the Predtechensky and Mayorov model for the case of a 500 Pa ambient.

Figure 15 Temporal evolution of the ablation plume for ions (a) and atoms (b) using a Gd metal sample under an 800 Pa He ambient and ablation energy of 0.5 mJ. The behavior of the inner component of the plume differs significantly between the oxide and metal samples.

Figure 16 Longitudinal fluorescence intensity distributions for ions (a) and atoms (b) using a Gd metal sample

under an 800 Pa He ambient and ablation energy of 0.5 mJ. The thickness of the hemispherical layer of atoms can be estimated to be 500 μm (full width at half maximum) at a delay time of 1 μs .

Figure 17 Dependence of the plume structure on He gas pressure for ions (a) and atoms (b) at a delay time of 0.5 μs and ablation energy of 0.5 mJ using a Gd oxide sample.

Figure 18 Plume structures for three gases (He, Ar, and Xe) for ions (a) and atoms (b) at a delay time of 1.0 μs and ablation energy of 0.15 mJ using a Gd oxide sample. The size of the inner cavity containing a reduced density of ablated species increases with decreasing mass of the ambient gas.

References

- [1] D. B. Chrisey, G. K. Hubler, Pulsed Laser Deposition of Thin Films, John Wiley & Sons, Inc., New York, 1994.
- [2] Y. Shimada, H. Nishimura, M. Nakai, K. Hashimoto, M. Yamaura, Y. Tao, K. Shigemori, T. Okuno, K. Nishihara, T. Kawamura, A. Sunahara, T. Nishikawa, A. Sasaki, K. Nagai, T. Norimatsu, S. Fujioka, S. Uchida, N. Miyanaga, Y. Izawa, C. Yamanaka, Characterization of extreme ultraviolet emission from laser-produced spherical tin plasma generated with multiple laser beams, *Appl. Phys. Lett.* 86 (2005) 051501.
- [3] D. A. Cremers, L. J. Radziemski, Handbook of Laser-Induced Breakdown Spectroscopy, John Wiley & Sons, Inc., New York, 2006.
- [4] R. E. Russo, X. Mao, H. Liu, J. Gonzalez, S. S. Mao, Laser ablation in analytical chemistry – a review, *Talanta* 57 (2002) 425-451.
- [5] S. J. Rehse, C. A. Ryder, Laser-induced breakdown spectroscopy for branching ratio and atomic lifetime measurements in singly-ionized neodymium and gallium, *Spectrochim. Acta B* 64 (2009) 974-980.
- [6] I. Schechter, V. Bulatov, Plasma morphology, in: A. W. Miziolek, V. Palleschi, I. Schechter (Eds.), *Laser induced breakdown spectroscopy*, Cambridge University Press, 2006, pp. 40-121.
- [7] V. I. Babushok, F. C. DeLucia, Jr, J. L. Gottfried, C. A. Munson, A. W. Miziolek, Double pulse laser ablation and plasma: laser induced breakdown spectroscopy signal enhancement, *Spectrochim. Acta B* 61 (2006) 999.
- [8] E. Tognoni, G. Cristoforetti, Basic mechanisms of signal enhancement in ns double-pulse laser-induced breakdown spectroscopy in a gas environment, *J. Anal. At. Spectrom.* 29 (2014) 1318-1338.
- [9] F. H. Kortenbruck, R. Noll, P. Wintjens, H. Falk, C. Becker, Analysis of heavy metals in soils using laser-induced breakdown spectrometry combined with laser-induced fluorescence, *Spectrochim. Acta B* 56 (2001) 933-945.
- [10] H. H. Telle, D. C. S. Beddows, G. W. Morris, O. Samek, Sensitive and selective spectrochemical analysis of metallic samples: the combination of laser-induced breakdown spectroscopy and laser-induced fluorescence spectroscopy, *Spectrochim. Acta B* 56 (2001) 947-960.
- [11] K. Rifai, F. Vidal, M. Chaker, M. Sabsabi, Resonant laser-induced breakdown spectroscopy (RLIBS) analysis of traces through selective excitation of aluminum in aluminum alloys, *J. Anal. At. Spectrom.* 28 (2013) 388-395.
- [12] S. L. Lui, N. H. Cheung, Resonance-enhanced laser-induced plasma spectroscopy: ambient gas effects, *Spectrochim. Acta B* 58 (2003) 1613-1623.
- [13] O. A. Nassef, H. E. Elsayed-Ali, Spark discharge assisted laser induced breakdown spectroscopy,

- Spectrochim. Acta B 60 (2005) 1564-1572.
- [14] Y. Liu, B. Bousquet, M. Baudelet, M. Richardson, Improvement of the sensitivity for the measurement of copper concentrations in soil by microwave-assisted laser-induced breakdown spectroscopy, *Spectrochim. Acta B* 73 (2012) 89-92.
- [15] M. Tampo, M. Miyabe, K. Akaoka, M. Oba, H. Ohba, Y. Maruyama, I. Wakaida, Enhancement of intensity in microwave-assisted laser-induced breakdown spectroscopy for remote analysis of nuclear fuel recycling, *J. Anal. At. Spectrom.* 29 (2014) 886-892.
- [16] K. Ali, M. Tampo, K. Akaoka, M. Miyabe, I. Wakaida, Enhancement of LIBS emission using antenna-coupled microwave, *Opt. Express* 21 (2013) 29755-29768.
- [17] I. B. Gornushkin, L. A. King, B. W. Smith, N. Omenetto, J. D. Winefordner, Line broadening mechanisms in the low pressure laser-induced plasma, *Spectrochim. Acta B* 54 (1992) 1207-1217.
- [18] H. Liu, A. Quentmeier, K. Niemax, Diode laser absorption measurement of uranium isotope ratios in solid samples using laser ablation, *Spectrochim. Acta B* 57 (2002) 1611-1623.
- [19] B. A. Bushaw, N. C. Anheier Jr., Isotope ratio analysis on micron-sized particles in complex matrices by laser ablation-absorption ratio spectrometry, *Spectrochim. Acta B* 64 (2009) 1259-1265.
- [20] M. Miyabe, M. Oba, H. Iimura, K. Akaoka, Y. Maruyama, H. Ohba, M. Tampo, I. Wakaida, Doppler-shifted optical absorption characterization of plume-lateral expansion in laser ablation of a cerium target, *J. Appl. Phys.* 112 (2012) 123303.
- [21] M. Miyabe, M. Oba, H. Iimura, K. Akaoka, Y. Maruyama, H. Ohba, M. Tampo, I. Wakaida, Absorption spectroscopy of uranium plasma for remote isotope analysis of next-generation nuclear fuel, *Appl. Phys. A* 112 (2013) 87-92.
- [22] M. Miyabe, M. Oba, H. Iimura, K. Akaoka, Y. Maruyama, I. Wakaida, Spectroscopy of laser-produced cerium plasma for remote isotope analysis of nuclear fuel, *Appl. Phys. A* 101 (2010) 65-70.
- [23] D. B. Geohegan, Fast intensified-CCD photography of $\text{YBa}_2\text{Cu}_3\text{O}_{7-x}$ laser ablation in vacuum and ambient oxygen, *Appl. Phys. Lett.* 60 (1992) 2732-2734.
- [24] A. Misra, A. Mitra, R. K. Thareja, Diagnostics of laser ablated plasmas using fast photography, *Appl. Phys. Lett.* 74 (1999) 929-931.
- [25] F. Kokai, K. Takahashi, M. Yudasaka, S. Iijima, Laser ablation of graphite-Co/Ni and growth of single-wall carbon nanotubes in vortexes formed in an Ar atmosphere, *J. Phys. Chem. B* 104 (2000) 6777-6784.
- [26] S. S. Harilal, C. V. Bindhu, M. S. Tillack, F. Najmabadi, A. C. Gaeris, Internal structure and expansion dynamics of laser ablation plumes into ambient gases, *J. Appl. Phys.* 93 (2003) 2380-2388.
- [27] C. Aragon, F. Penalba, J. A. Aguileral, Spatial characterization of laser-induced plasmas: distributions

- of neutral atom and ion densities, *Appl. Phys. A* 79 (2004) 1145-1148.
- [28] D. Grojo, J. Hermann, A. Perrone, Plasma analyses during femtosecond laser ablation of Ti, Zr, and Hf, *J. Appl. Phys.* 97 (2005) 063306.
- [29] X. Bai, Q. Ma, M. Perrier, V. Motto-Ros, D. Sabourdy, L. Nguyen, A. Jalocha, J. Yu, Experimental study of laser-induced plasma: influence of laser fluence and pulse duration, *Spectrochim. Acta B* 87 (2013) 27-35.
- [30] C. Aragon, J. A. Aguilera, Characterization of laser induced plasmas by optical emission spectroscopy: A review of experiments and methods, *Spectrochim. Acta B* 63 (2008) 893-916.
- [31] R. M. Gilgenbach, P. L. G. Ventzeck, Dynamics of excimer laser-ablated aluminum neutral atom plume measured by dye laser resonance absorption photography, *Appl. Phys. Lett.* 58 (1991) 1597-1599.
- [32] M. A. Cappelli, P. H. Paul, R. K. Hanson, Laser-induced fluorescence imaging of laser-ablated barium, *J. Appl. Phys.* 56 (1990) 1715-1717.
- [33] A. D. Sappey, T. K. Gamble, Planar laser-induced fluorescence imaging of Cu atom and Cu₂ in a condensing laser-ablated copper plasma plume, *J. Appl. Phys.* 72 (1992) 5095-5107.
- [34] G. W. Martin, L. A. Doyle, A. Al-Khateeb, I. Weaver, D. Riley, M.J. Lamb, T. Morrow, C.L.S. Lewis, Three-dimensional number density mapping in the plume of a low-temperature laser-ablated magnesium plasma, *Appl. Surf. Sci.* 127-129 (1998) 710-715.
- [35] C. Dutouquet, J. Hermann, Laser-induced fluorescence probing during pulsed-laser ablation for three-dimensional number density mapping of plasma species, *J. Phys. D: Appl. Phys.* 34 (2001) 3356-3363.
- [36] Y. Nakata, H. Kaibara, T. Okada, M. Maeda, Two-dimensional laser-induced fluorescence imaging of a pulsed-laser deposition process of YBa₂Cu₃O_{7-x}, *J. Appl. Phys.* 80 (1996) 2458-2466.
- [37] K. Sasaki, S. Matsui, H. Ito, K. Kadota, Dynamics of laser-ablation Ti plasmas studied by laser-induced fluorescence imaging spectroscopy, *J. Appl. Phys.* 92 (2002) 6471-6476.
- [38] S. A. Ahmad, A. Venugopalan and G. D. Saksena, Isotope shifts in odd and even energy levels of the neutral and singly ionised gadolinium atom, *Spectrochim. Acta* 34B (1979) 221-235.
- [39] M. Miyabe, M. Oba and I. Wakaida, Analysis of even-parity Rydberg series of Gd I to determine its ionization potential and isotope shift, *J. Phys. B* 31 (1998) 4559-4571.
- [40] S. A. Ahmad, A. Venugopalan and G. D. Saksena, Isotope shifts in odd and even energy levels of the neutral and singly ionised gadolinium atom, *Spectrochim. Acta* 34B (1979) 221-235.
- [41] N. Taylor, N. Omenetto, B. W. Smith and J. D. Winefordner, Time-resolved laser-induced saturated fluorescence measurements in a thallium see-through hollow cathode discharge: Evaluation of ground state number density and quantum efficiency, *J. Quant. Spectrosc. Rad. Trans.* 109 (2008) 2561-2578.
- [42] T. E. Itina, J. Hermann, Ph. Delaporte, M. Sentis, Laser-generated plasma plume expansion: Combined

- continuous-microscopic modeling, *Phys. Rev. E* 66 (2002) 066406.
- [43] A. V. Bulgakov, N. M. Bulgakova, Gas-dynamic effects of the interaction between a pulsed laser-ablation plume and the ambient gas: analogy with an underexpanded jet, *J. Phys. D: Appl. Phys.* 31 (1998) 693-703.
- [44] A. V. Bulgakov, M. R. Predtechensky, A. P. Mayorov, Transport of neutral atoms, monoxides, and clusters in the plume produced by laser ablation of $\text{YBa}_2\text{Cu}_3\text{O}_{7-x}$ in oxygen environment, *Appl. Surf. Sci.* 96-98 (1996) 159-163.
- [45] J. Gonzalo, C. N. Afonso I. Madariaga, Expansion dynamics of the plasma produced by laser ablation of BaTiO_3 in a gas environment, *J. Appl. Phys.* 81 (1997) 951-955.
- [46] T. E. Itina, J. Hermann, Ph. Delaporte, M. Sentis, Combined continuous–microscopic modeling of laser plume expansion, *Appl. Surf. Sci.* 208-209 (2003) 27-32.
- [47] M. Han, Y. Gong, J. Zhou, C. Yin, F. Song, N. Muto, T. Takiya, Y. Iwata, Plume dynamics during film and nanoparticles deposition by pulsed laser ablation, *Phys. Lett. A* 302 (2002) 182–189.
- [48] A. Bogaerts, Z. Chen, D. Bleiner, Laser ablation of copper in different background gases: comparative study by numerical modeling and experiments, *J. Anal. At. Spectrom.* 21 (2006) 384-395.
- [49] Y. Yamagata, K. Shingai, A. M. Grishin, T. Ikegami, K. Ebihara, Spectroscopic study of the YBCO ablation plasma plume: crossover the “blast” to the “drag” regime, *Thin Solid Film* 316 (1998) 56-59.
- [50] B. D. Ngom, S. Lafane, A. Dioum, N. Manyala, S. Abdelli-Messaci, R. T. Kerdja, R. Madjioe, R. Nemutudi, M. Maaza, A. C. Beye, The influence of plasma dynamics on the growth of $\text{Sm}_{0.55}\text{Nd}_{0.45}\text{NiO}_3$ solid solution during pulsed laser deposition, *J. Phys. Chem. Solid* 72 (2011) 1218-1224.
- [51] R. F. Wood, K. R. Chen, J. N. Leboeuf, A. A. Puretzky, D. B. Geohegan, Dynamics of plume propagation and splitting during pulsed-laser ablation, *Phys. Rev. Lett.* 79 (1997) 1571-1574.
- [52] S. Amoruso, J. Schou, J. G. Lunney, Multiple-scattering effects in laser ablation plume propagation in gas, *Europhys. Lett.* 76 (2006) 436-442.
- [53] M. R. Predtechensky, A. P. Mayorov, Expansion of laser plasma in oxygen at laser deposition of HTSC films: Theoretical model, *Appl. Supercond.* 1 (1993) 2011-2017.
- [54] S. Amoruso, J. Schou, J. G. Lunney, Influence of the atomic mass of the background gas on laser ablation plume propagation, *Appl. Phys. A* 92 (2008) 907-911.
- [55] N. Arnold, J. Gruber, J. Heitz, Spherical expansion of the vapor plume into ambient gas: an analytical model, *Appl. Phys. A* 69 (1999) S87-S93.
- [56] N. M. Bulgakova, A. V. Bulgakov, O. F. Bobrenok, Double layer effects in laser-ablation plasma plumes, *Phys. Rev. E* 62 (2000) 5624-5635.
- [57] R. Kelly, R. W. Dreyfus, On the effect of Knudsen-layer formation on studies of vaporization, sputtering and desorption, *Surf. Sci.* 198 (1988) 263-276.

- [58] Q. Ma, V. Motto-Ros, X. Bai, J. Yu, Experimental investigation of the structure and the dynamics of nanosecond laser-induced plasma in 1-atm argon ambient gas, *Appl. Phys. Lett.* 103 (2013) 204101.
- [59] N. R. Taylor, M. C. Phillips, Differential laser absorption spectroscopy of uranium in an atmospheric pressure laser-induced plasma, *Opt. Lett.* 39 (2014) 594-597.
- [60] Y. Hahn, Electron-ion recombination processes – an overview, *Rep. Prog. Phys.* 60 (1997)691-759.
- [61] S. Namba, R. Nozu, K. Takiyama, Spectroscopic study of ablation and recombination processes in a laser-produced ZnO plasma, *J. Appl. Phys.* 99 (2006) 073302.
- [62] A. De Giacomo, Experimental characterization of metallic titanium-laser induced plasma by time and space resolved optical emission spectroscopy, *Spectrochim Acta B* 58 (2003) 71-83.
- [63] J. A. Aguilera, C. Aragon, Temperature and electron density distributions of laser-induced plasmas generated with an iron sample at different ambient gas pressures, *Appl. Surf. Sci.* 197-198 (2002) 273-280.
- [64] A. De Giacomo, M. Dell'Aglio, R. Gaudiuso, G. Cristoforetti, S. Legnaioli, V. Palleschi, E. Tognoni, Spatial distribution of hydrogen and other emitters in aluminum laser-induced plasma in air and consequences on spatially integrated laser-induced breakdown spectroscopy measurements, *Spectrochim Acta B* 63 (2008) 980-987.
- [65] <http://www.cfa.harvard.edu/amp/ampdata/kurucz23/sekur.html>
- [66] Z. G. Zhang, A. Persson, Z. S. Li, S. Svanberg, J. Zhankui, Lifetime measurements in Gd II and Gd III using time-resolved laser spectroscopy, *Eur. Phys. J. D* 13 (2001) 301-304.
- [67] Q. Wang, L. Jiang, H. Jiang, X. Shang, Y. Tian, Z. Dai, Radiative lifetime measurements of some Gd I and Gd II levels using time-resolved laser spectroscopy, *J. Phys. B* 46 (2013) 045003.
- [68] E. A. Den Hartog, K. A. Bilty, J. E. Lawler, Radiative lifetimes of neutral gadolinium, *J. Phys. B* 44 (2011) 055001.

Table 1 Spectroscopic data relevant to the present study

5th and 11th columns denote lower level energies and 6th and 12th columns denote total angular momentum of the lower level [65], and third and 9th columns denote branching ratios of the corresponding transitions. In the ratio calculation, lifetime data from ref. [66] for Gd ion and ref. [67] for Gd atom were used. The lifetime for 31869 cm⁻¹ level of Gd atoms was also reported to be 7.1 ns in ref. [68].

(a) Gd atom						(b) Gd ion					
31869.139 cm ⁻¹ (Ju=3)						32262.787 cm ⁻¹ (Ju=3.5)					
Wavelength	<i>gf</i>	BR	A	lower level	<i>J</i>	Wavelength	<i>gf</i>	BR	A	lower level	<i>J</i>
air (nm)			x10 ⁷ (1/s)	(cm ⁻¹)		air (nm)			x10 ⁷ (1/s)	(cm ⁻¹)	
313.692	0.54	0.24	5.27	0.00	2	309.865	0.22	0.10	1.94	0.00	2.5
319.028	0.66	0.28	6.21	532.98	4	312.400	0.18	0.09	1.58	261.84	3.5
411.294	0.42	0.11	2.36	7562.46	2	316.069	0.07	0.03	0.60	633.27	4.5
476.383	1.30	0.25	5.47	10883.51	4	342.593	0.26	0.10	1.82	3082.01	2.5
495.315	0.73	0.13	2.85	11685.59	4	346.695	0.22	0.08	1.56	3427.27	3.5
						346.899	1.16	0.43	8.04	3444.24	3.5
						356.404	0.15	0.05	0.97	4212.76	2.5
						432.407	0.17	0.04	0.77	9142.90	3.5
						513.027	0.14	0.02	0.45	12776.07	2.5
						516.089	0.10	0.02	0.32	12891.69	3.5
						521.048	0.13	0.02	0.39	13076.05	4.5
1.00						1.00					

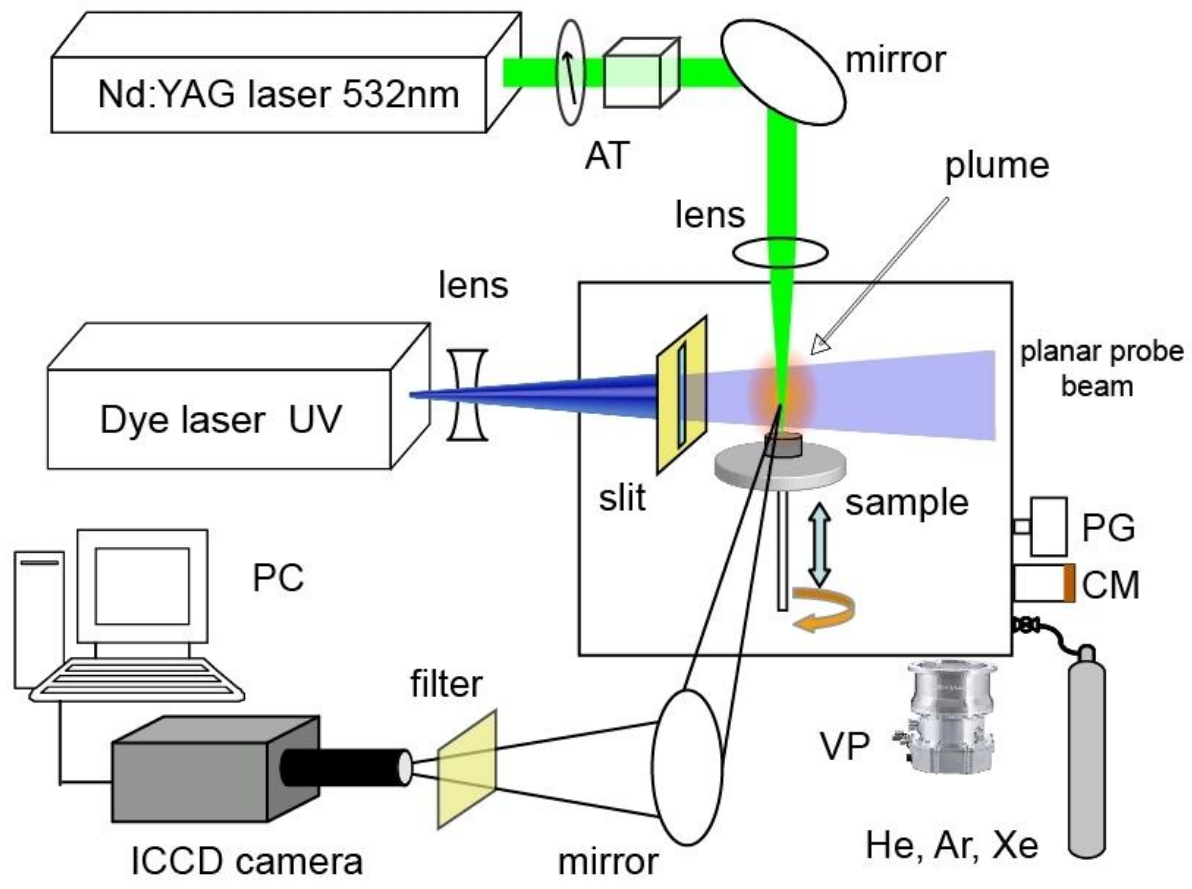
Table 2 Intense emission transitions transmitted through optical filters utilized

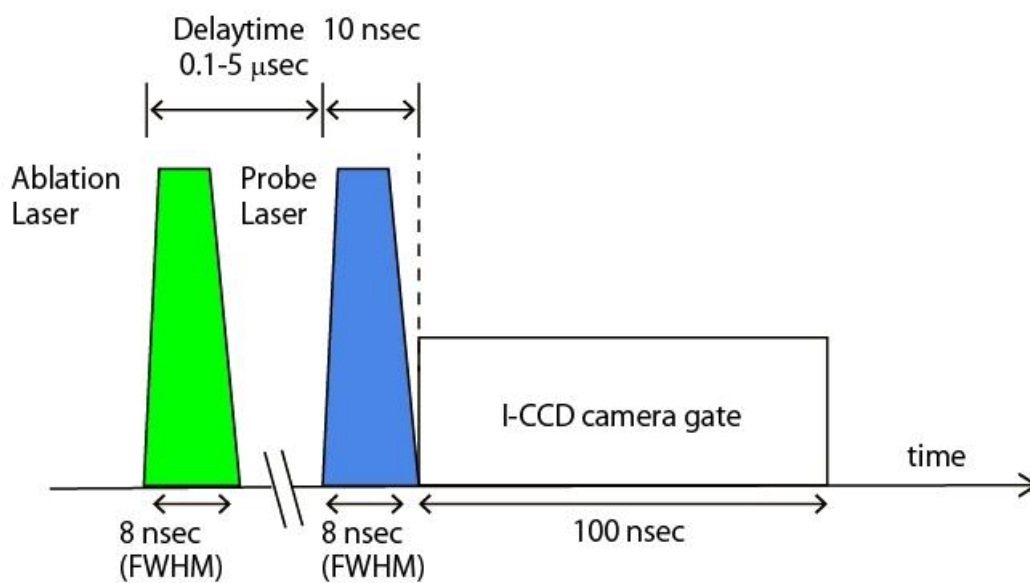
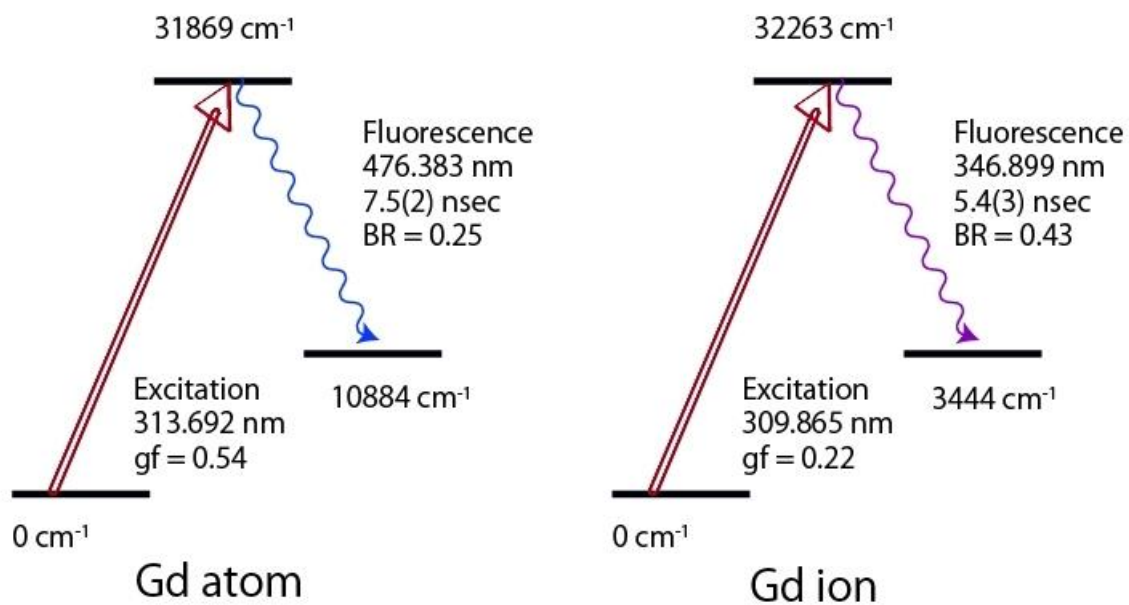
All data are taken from [65]

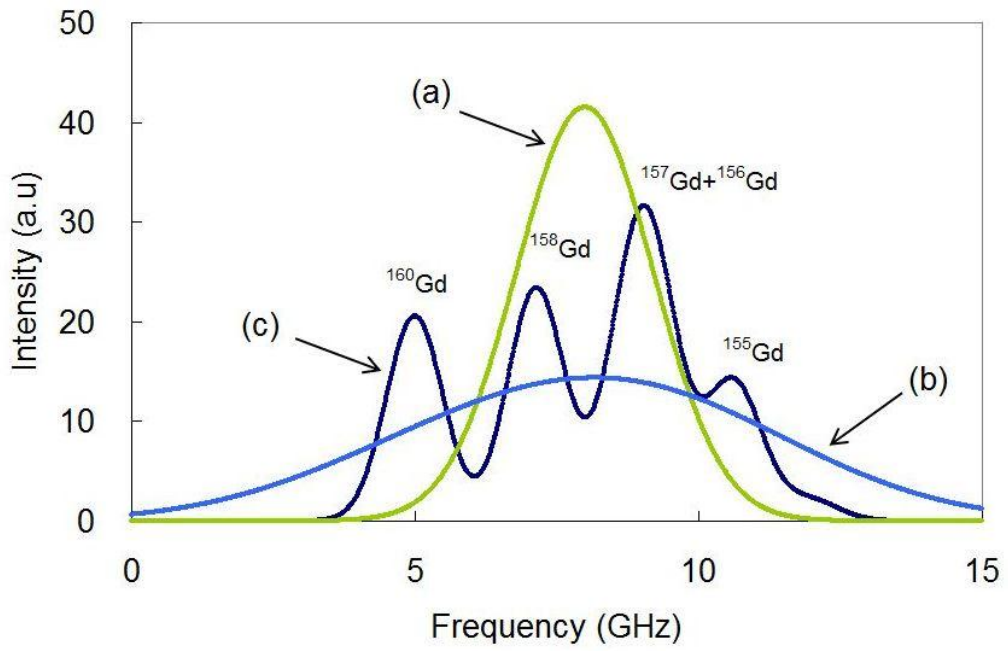
(a) 480nm Filter for atom					(b) 350nm Filter for ion				
Wavelength in air (nm)	A $\times 10^7(1/s)$	Species	Lower level (cm^{-1})	Upper level (cm^{-1})	Wavelength in air (nm)	A $\times 10^7(1/s)$	Species	Lower level (cm^{-1})	Upper level (cm^{-1})
475.550	5.10	Gd II	20369.257	41391.647	345.124	9.75	Gd II	3082.011	32048.837
475.870	3.63	Gd I	7103.420	28111.670	346.399	10.32	Gd II	3444.235	32304.409
476.383	5.47	Gd I	10883.505	31869.139	346.727	10.71	Gd II	3427.274	32260.120
476.725	4.81	Gd I	7480.348	28450.948	346.899	8.04	Gd II	3444.235	32262.787
478.098	2.35	Gd I	11296.465	32206.820	348.128	8.60	Gd II	4841.106	33557.951
478.464	2.91	Gd I	7947.294	28841.676	348.180	7.27	Gd II	3972.167	32684.712
478.676	4.35	Gd I	12345.966	33231.096	350.551	7.13	Gd II	3972.167	32490.510
480.801	3.32	Gd I	13926.311	34719.128	351.250	20.72	Gd II	10091.567	38553.210
482.994	2.22	Gd I	11685.594	32384.000	351.677	7.86	Gd II	11669.863	40096.902
484.810	3.46	Gd I	12345.966	32966.862	354.936	6.83	Gd II	1935.310	30101.366

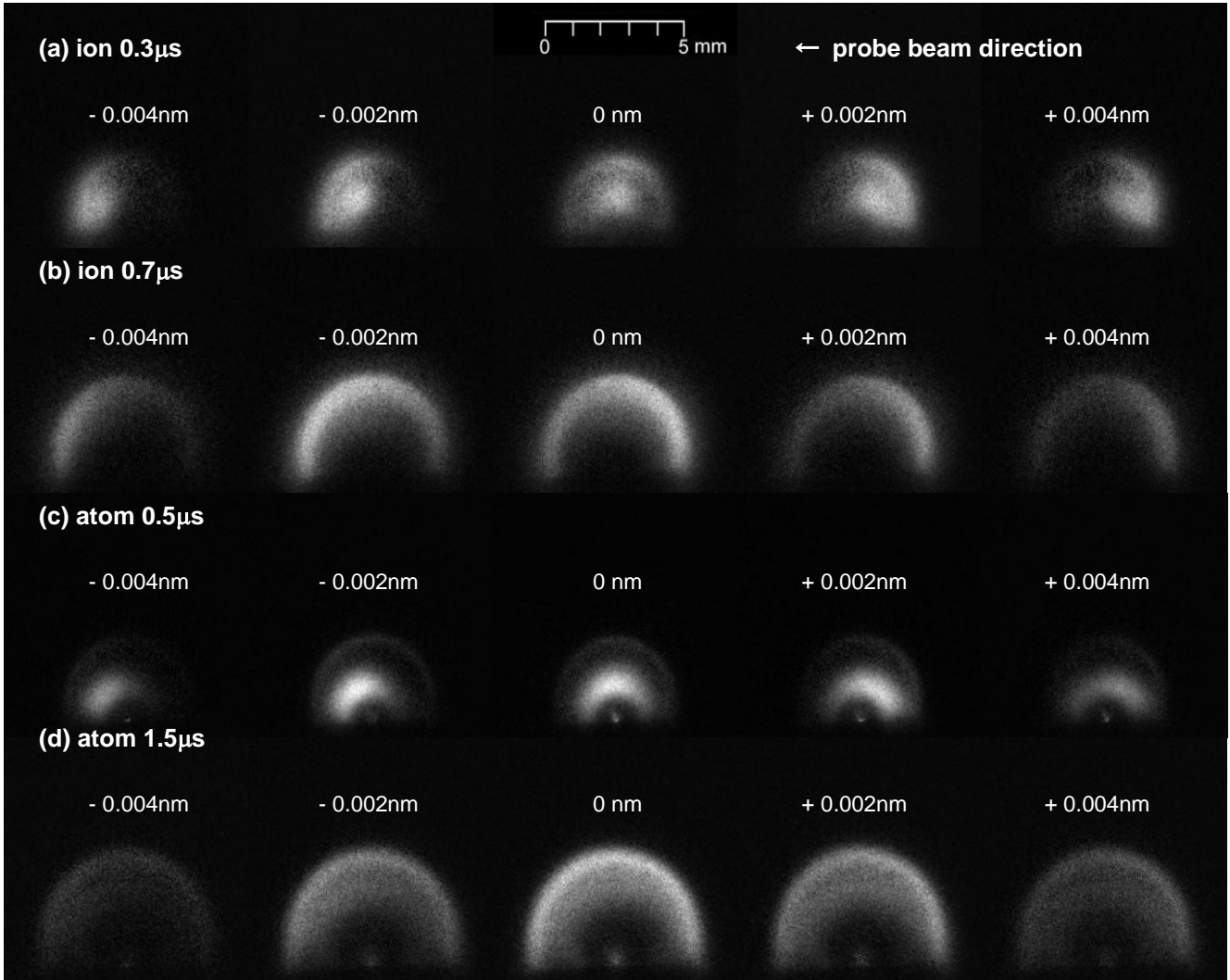
Table 3 Fitting parameters of drag model for lateral and longitudinal plume evolution
 d_f is in mm and β is in $1/\mu\text{s}$.

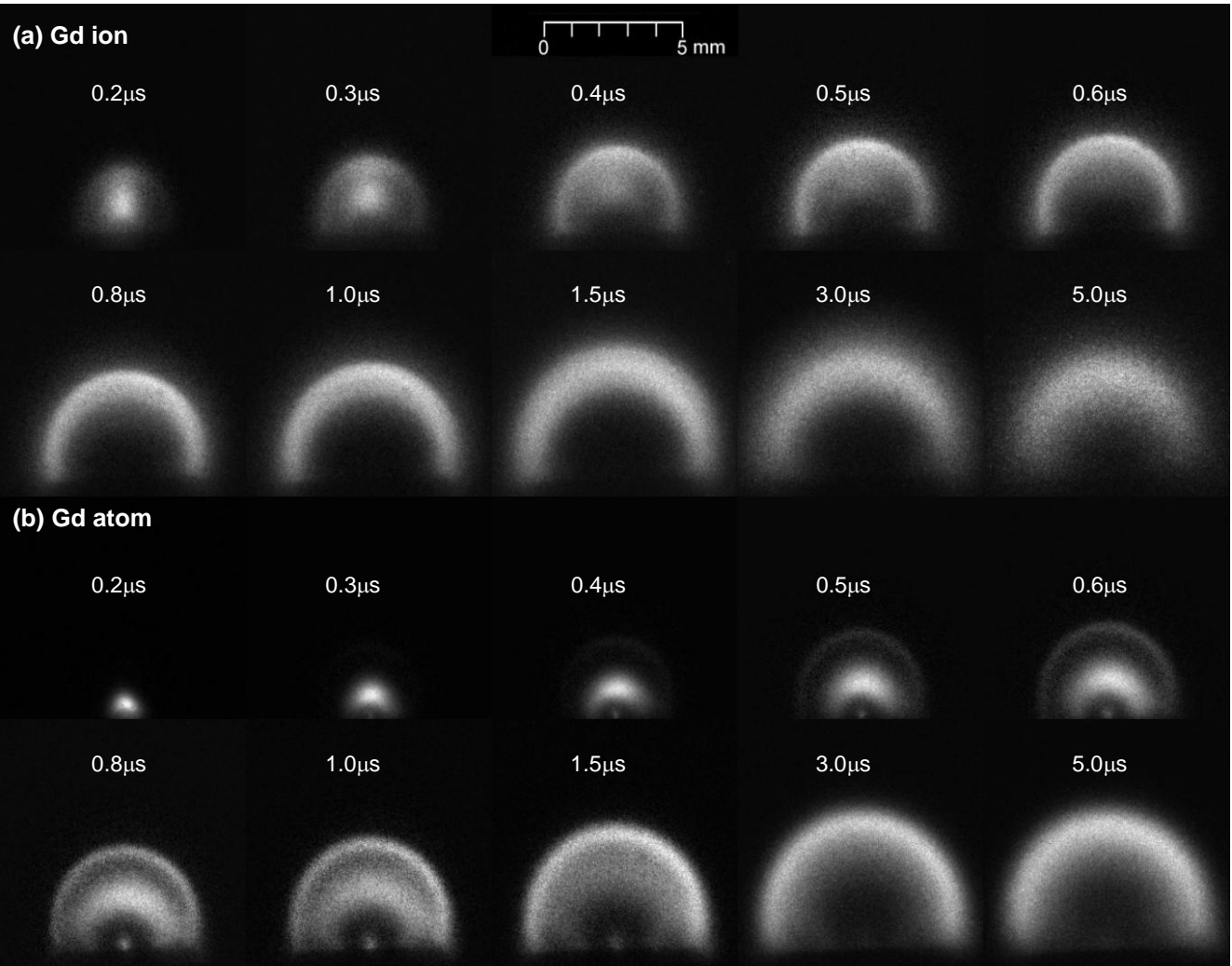
Pressure (Pa)	longitudinal				lateral	
	outer layer		inner component		outer layer	
	d_f	β	d_f	β	d_f	β
	<i>0.15mJ</i>					
800	2.8	2.8	3.4	1.0	2.0	2.1
	<i>0.5mJ</i>					
1300	3.3	3.2	4.7	0.57	2.4	3.2
800	4.3	2.7	5.8	0.49	3.1	2.4
500	5.2	1.9	7.3	0.41	4.1	1.5
300	6.4	1.4	8.9	0.34	5.2	1.1
200	7.7	1.1	12.0	0.25	7.7	0.6

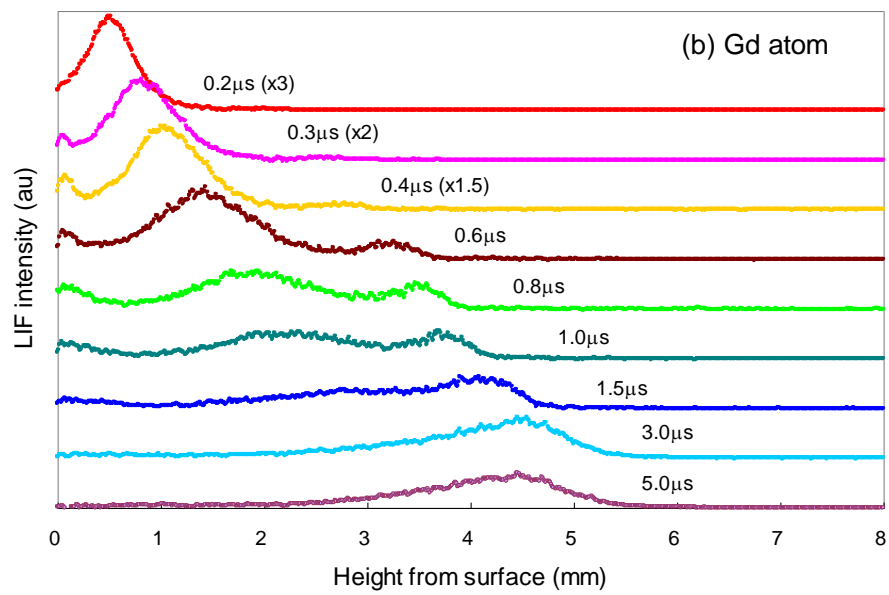
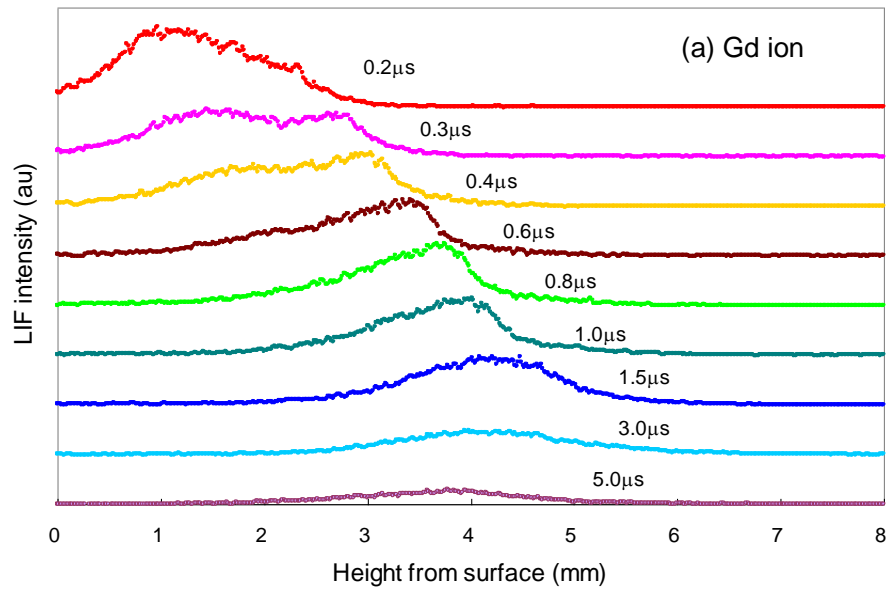


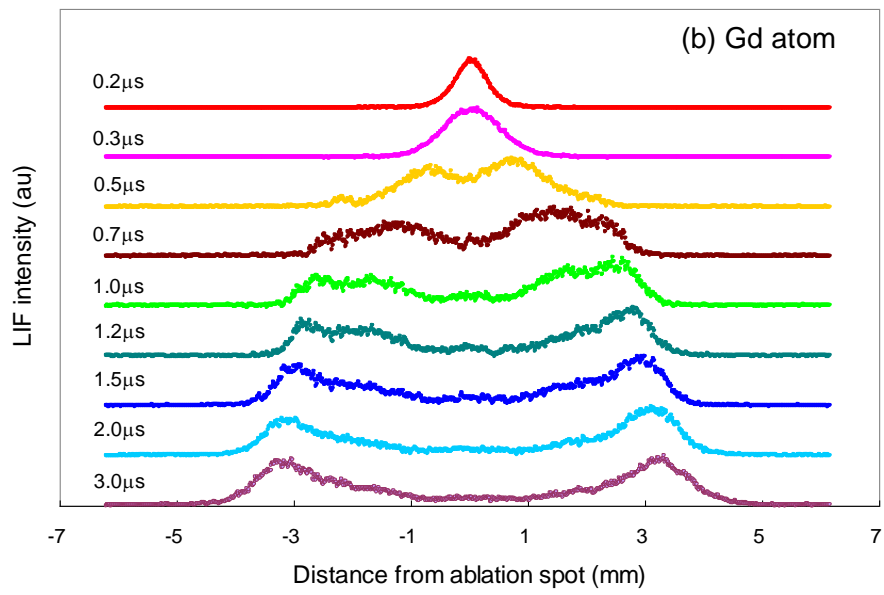
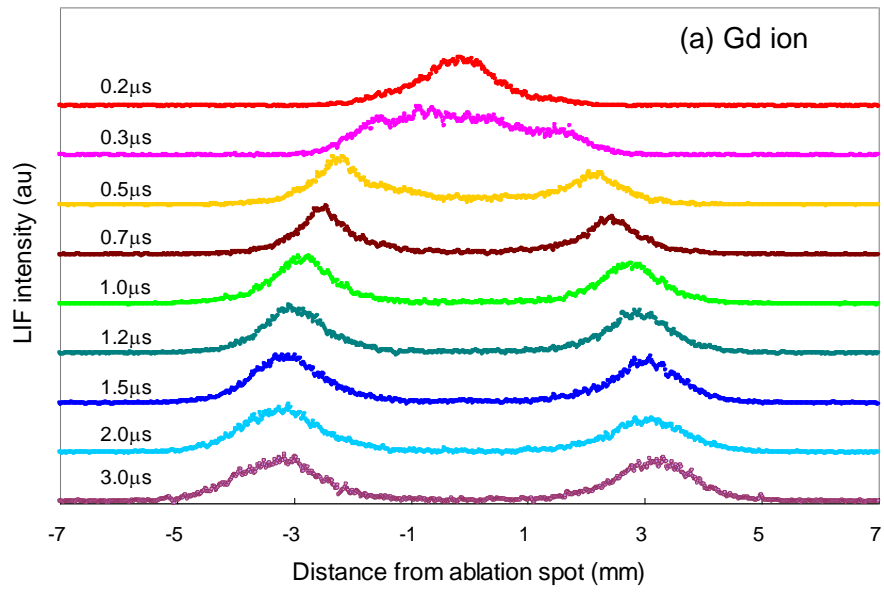


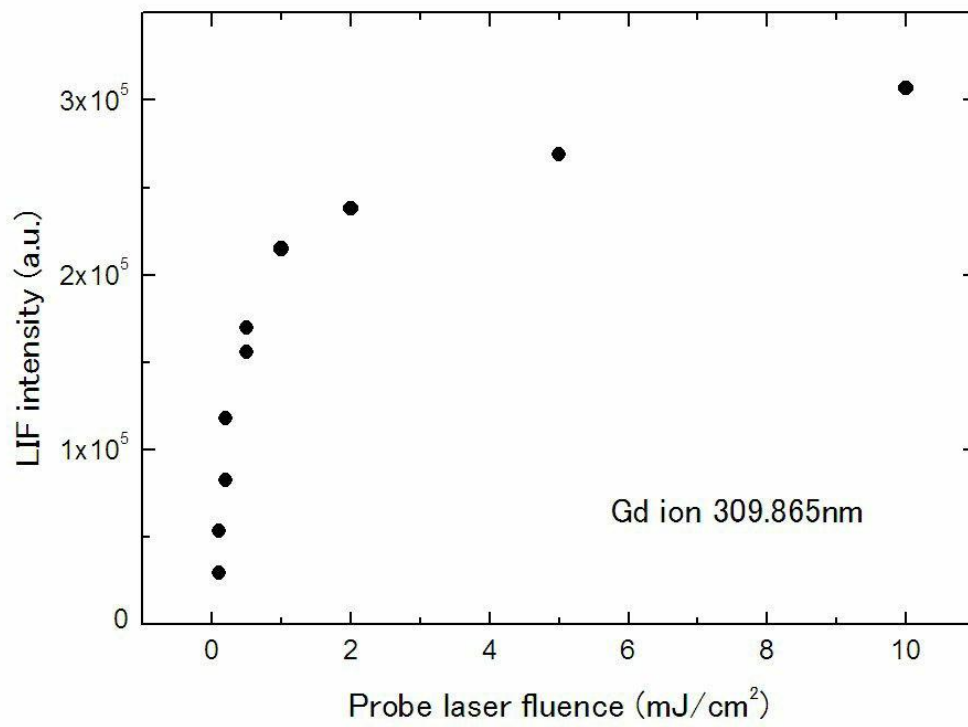


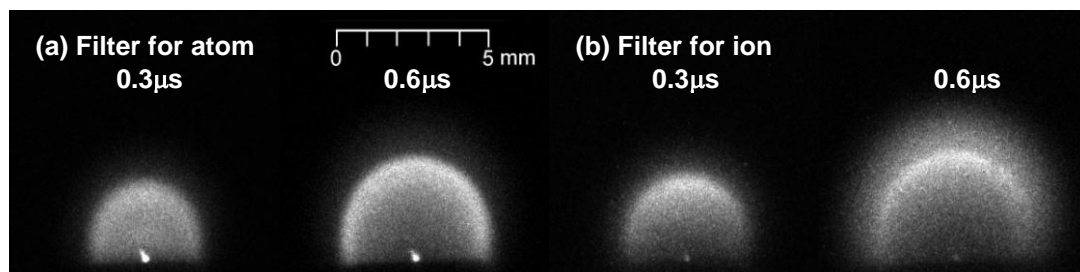


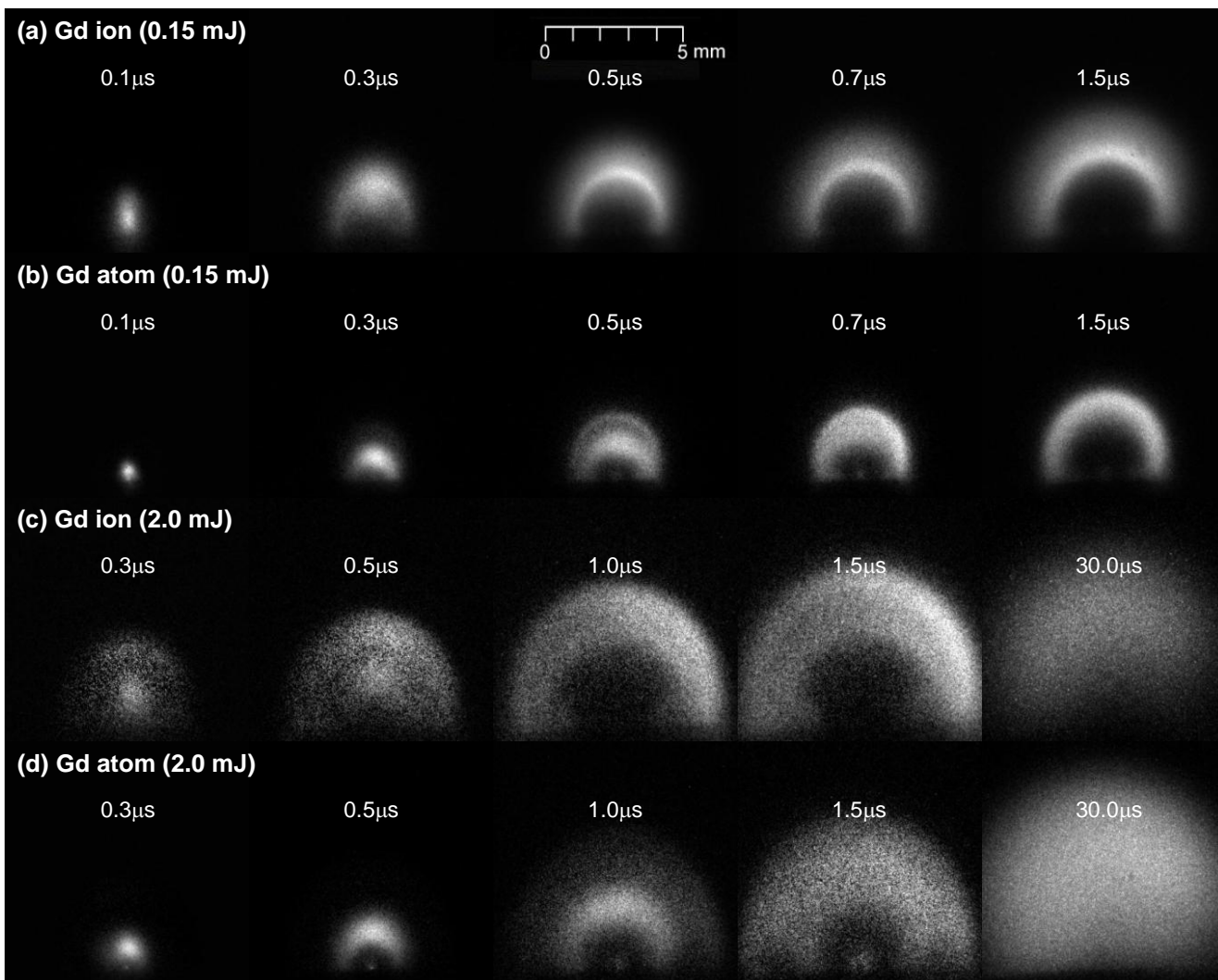


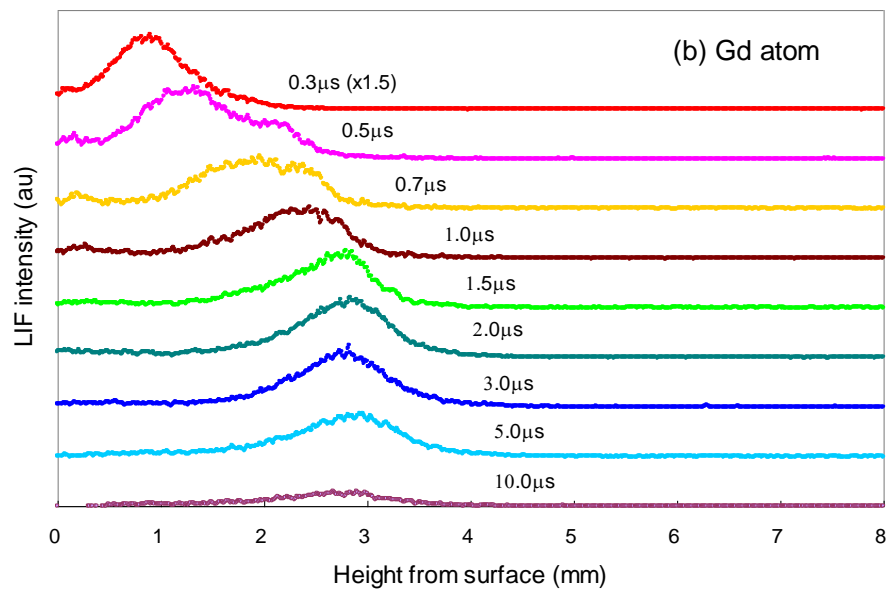
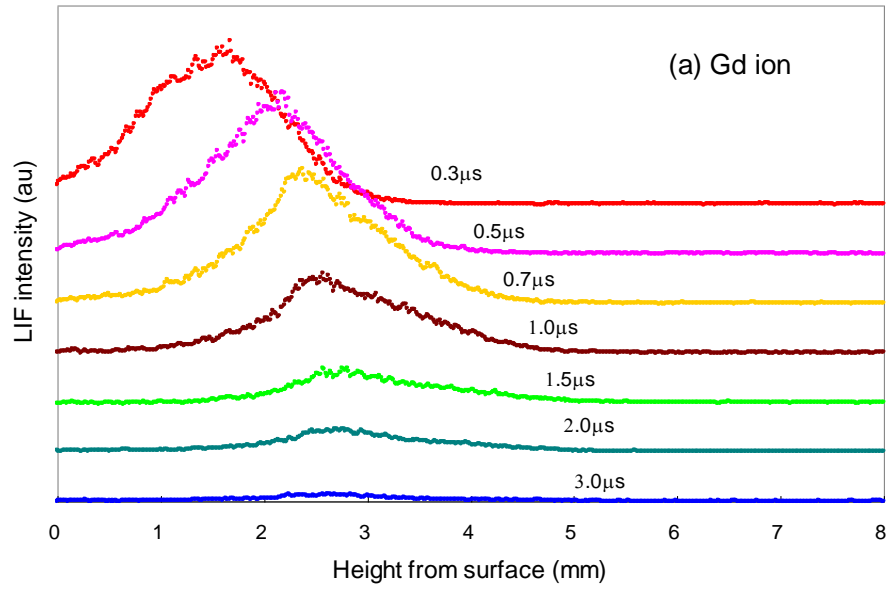


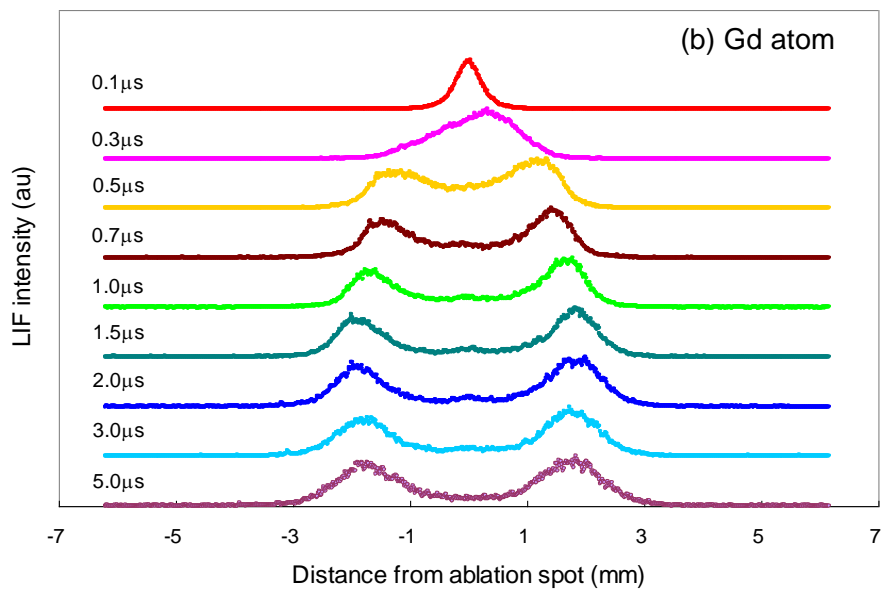
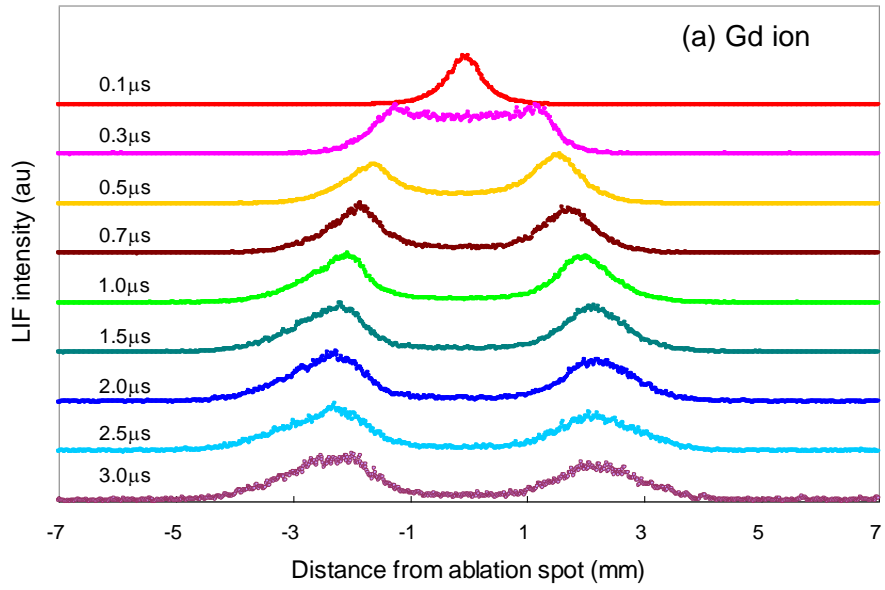


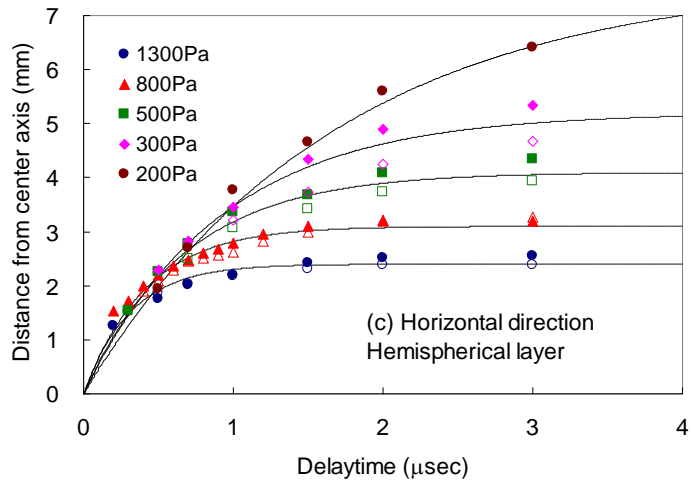
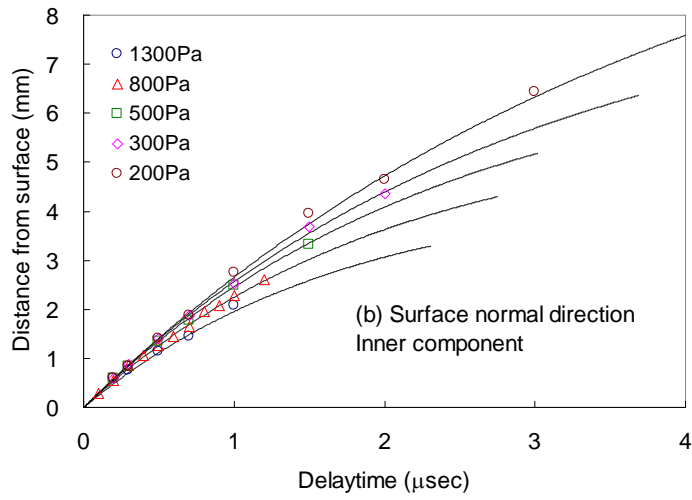
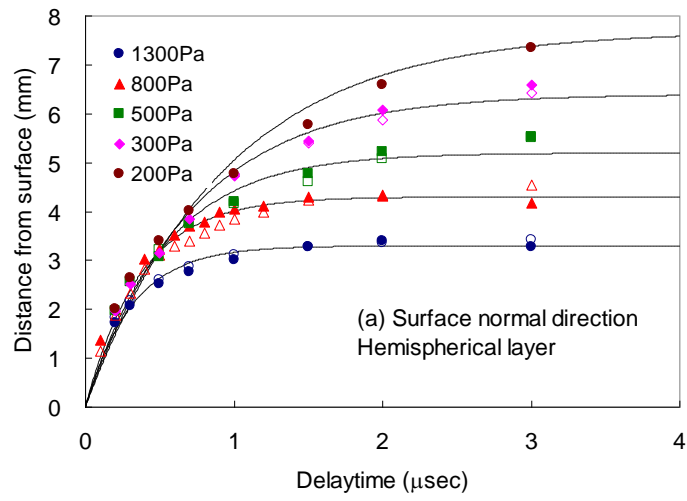


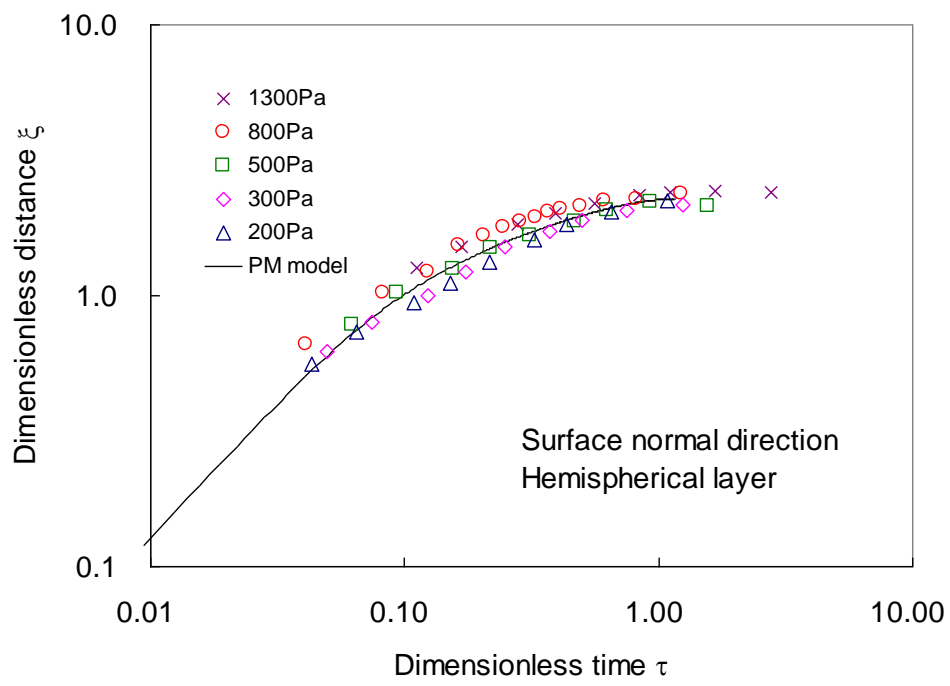


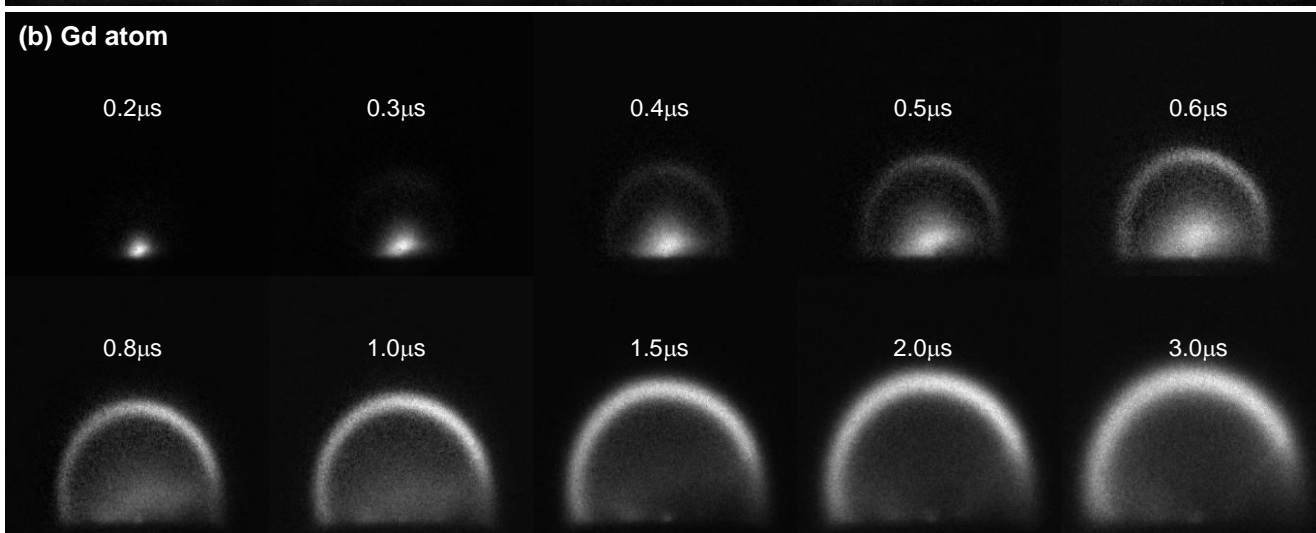
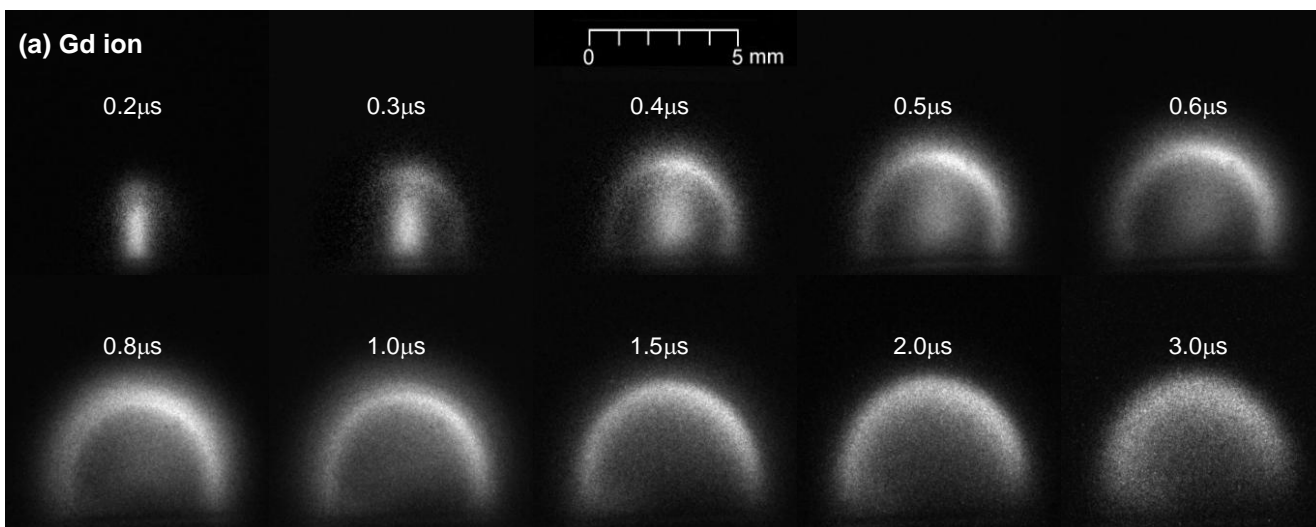


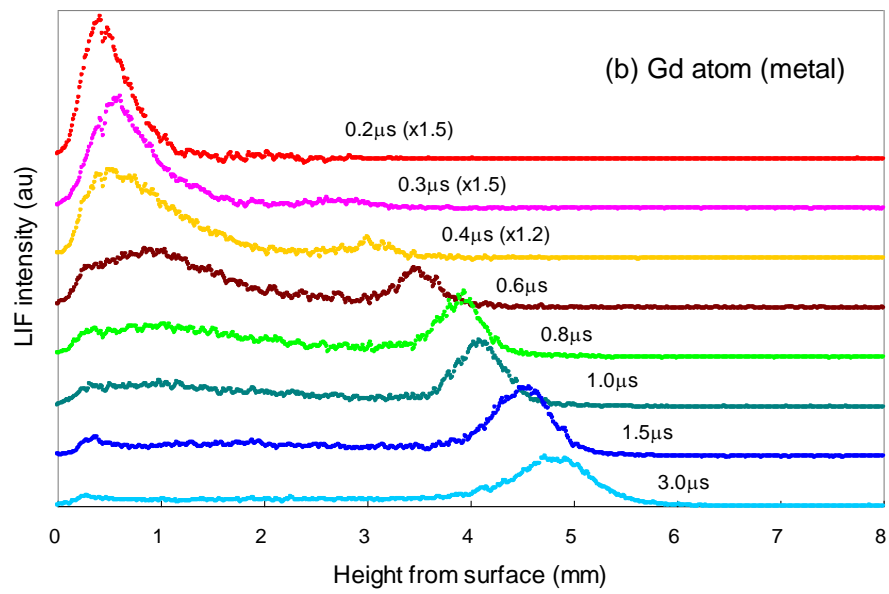
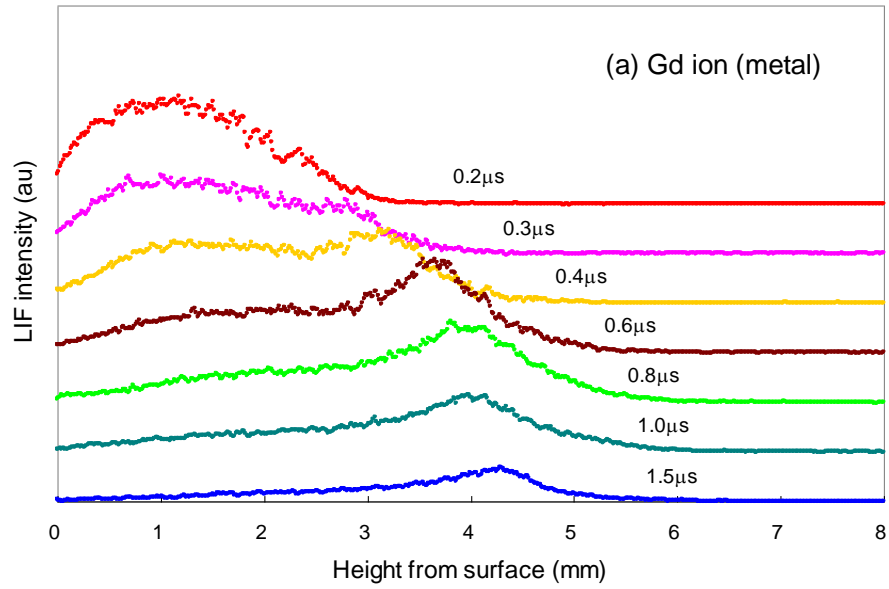




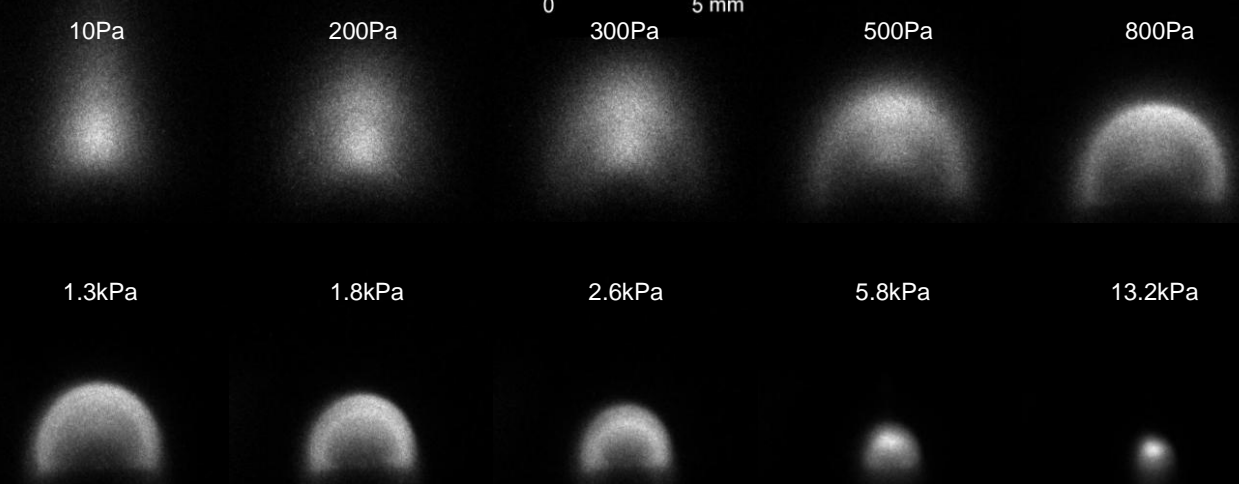




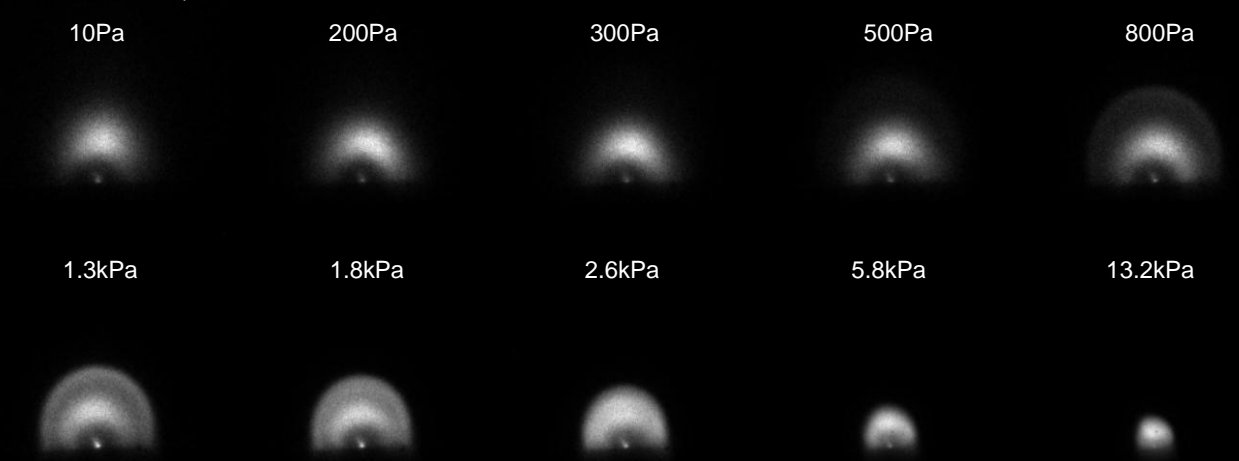




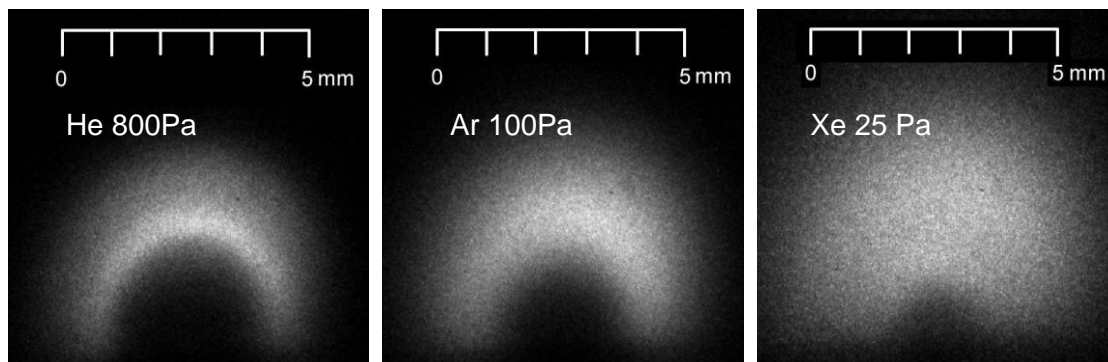
(a) Gd ion (0.5 μ s)



(b) Gd atom (0.5 μ s)



(a) Gd ion



(b) Gd atom

